

INTERIM REPORT

Morphology and Mechanism of Benign Inhibitors

SERDP Project WP-1619

JANUARY 2009

Dale W. Schaefer
Peng Wang
Xuecheng Dong
University of Cincinnati

This document has been cleared for public release



REPORT DOCUMENTATION PAGE				Form Approved OMB No. 0704-0188	
<p>The public reporting burden for this collection of information is estimated to average 1 hour per response, including the time for reviewing instructions, searching existing data sources, gathering and maintaining the data needed, and completing and reviewing the collection of information. Send comments regarding this burden estimate or any other aspect of this collection of information, including suggestions for reducing the burden, to the Department of Defense, Executive Services and Communications Directorate (0704-0188). Respondents should be aware that notwithstanding any other provision of law, no person shall be subject to any penalty for failing to comply with a collection of information if it does not display a currently valid OMB control number.</p> <p>PLEASE DO NOT RETURN YOUR FORM TO THE ABOVE ORGANIZATION.</p>					
1. REPORT DATE (DD-MM-YYYY) 02/02/2009		2. REPORT TYPE Final		3. DATES COVERED (From - To) 01/28/2008 - 01/29/2009	
4. TITLE AND SUBTITLE Morphology and Mechanism in Benign Inhibitors				5a. CONTRACT NUMBER W912HQ-08-P0015	
				5b. GRANT NUMBER G100997-7200300000-1-1005966	
				5c. PROGRAM ELEMENT NUMBER	
6. AUTHOR(S) Schaefer, Dale W. Wang, Peng Dong, Xuechen				5d. PROJECT NUMBER WP-1619	
				5e. TASK NUMBER	
				5f. WORK UNIT NUMBER	
7. PERFORMING ORGANIZATION NAME(S) AND ADDRESS(ES) University of Cincinnati Office of Sponsored Research Services 51 Goodman Drive, PO Box 21022, Cincinnati, OH 45221-0222				8. PERFORMING ORGANIZATION REPORT NUMBER	
9. SPONSORING/MONITORING AGENCY NAME(S) AND ADDRESS(ES) USACE, HUMPHREYS ENGR CTR SPT ACTIVITY ATTN: CEHEC-CT 7701 Telegraph Road Alexandria VA 22315-3660				10. SPONSOR/MONITOR'S ACRONYM(S) USACE	
				11. SPONSOR/MONITOR'S REPORT NUMBER(S)	
12. DISTRIBUTION/AVAILABILITY STATEMENT					
13. SUPPLEMENTARY NOTES					
14. ABSTRACT <p>Neutron and x-ray reflectivity are used to determine the composition profile of vanadate and trivalent chromium process (TCP) inhibitor films. In both cases, the films have a complex structure consisting of at least two layers. For vanadate films, a porous, hydrophilic layer exists at the interface between the film and the metal substrate. For TCP films, the interfacial layer is very thin and dense if the film is deposited electrochemically. The films also differ in hydration. Vanadate films are un-hydrated whereas TCP films exist as hydrates of the form $\text{Cr}_2\text{O}_3 \cdot 4\text{H}_2\text{O}$. In both cases, the bulk of the films is not fully dense. Densification is observed, however, at high temperature and when dried after exposure to liquid water. The differences in film morphology imply different mechanisms of film formation. Mechanisms are described that are consistent with the observations.</p>					
15. SUBJECT TERMS corrosion, inhibitors, mechanism, reflectivity, aluminum					
16. SECURITY CLASSIFICATION OF:			17. LIMITATION OF ABSTRACT	18. NUMBER OF PAGES 49	19a. NAME OF RESPONSIBLE PERSON Dale W. Schaefer
a. REPORT	b. ABSTRACT	c. THIS PAGE			19b. TELEPHONE NUMBER (Include area code) 513 556 5431

Table of Contents

List of Tables	iv
List of Figures	v
List of Acronyms	viii
List of All Film Systems Analyzed.....	3
Acknowledgement	ix
Section 1. Executive Summary	1
Section 2. Objective	4
Section 3. Background	4
Section 4. Materials and Methods.....	6
4.1 Metal substrates.....	6
4.1.1 Silicon wafer	6
4.1.2 Pure Aluminum substrate.....	6
4.1.3 Pure Copper substrate	6
4.1.4 Aluminum alloy (AA2024) substrate.....	6
4.1.5 Substrate preparation	6
4.1.6 Structure of AA2024 substrate.....	7
4.1.7 Optimization of the metal substrate	7
4.2 Characterization Methods	7
4.2.1 Neutron reflectivity (NR) and x-ray reflectivity (XR).....	7
4.2.2 X-ray diffraction	8
4.3 Vanadate inhibition system	8
4.3.1 Formulation.....	8
4.3.2 Film growth procedure.....	9
4.3.3 Film study methods.....	9
4.4 Trivalent chromium processing (TCP) system.....	12
4.4.1 Formulation.....	12
4.4.2 Film growth procedure.....	12
4.4.3 Response to high temperature (150 °C)	12
4.4.4 Salt solution aging.....	13
4.5 Cerium inhibition system	13

4.5.1	Formulation.....	13
4.5.2	Film growth procedure.....	13
4.6	Zinc phosphate inhibition system (ZP system)	14
4.6.1	Formulation.....	14
4.6.2	Film growth procedure.....	14
Section 5. Results and Accomplishments		15
5.1	Substrate morphology	15
5.1.1	Objective and technical approach	15
5.1.2	Project Accomplishments	15
5.2	Inhibitor film structure	18
5.2.1	Vanadate inhibitor films (V films).....	18
5.2.2	V film on Cu substrate	26
5.2.3	Trivalent chromium process films (TCP films)	26
5.2.4	Ce and ZP conversion coating films	34
Section 6. Conclusions.....		35
6.1	Conclusions regarding substrate preparation	35
6.2	Conclusions regarding Vanadate (V) films	35
6.3	Conclusions regarding TCP films	36

List of Tables

Table 1. SLD and density of TCP film layer by immersion	28
Table 2. Thickness, neutron SLD and density of TCP ($\text{Cr}(\text{OH})_3 \cdot n\text{H}_2\text{O}$) by EA-deposition.....	31
Table 3. Thickness, SLD of TCP EA-deposition film before and after baking.....	33
Table 4. Thickness, SLD and density of TCP ($\text{Cr}(\text{OH})_3 \cdot 0.5\text{H}_2\text{O}$) by EA-deposition.....	34

List of Figures

Figure 1. Experimental setup for specular NR/XR measurement in as-prepared dry state.	7
Figure 2. Experimental set up for “ <i>vapor conditioning</i> ” experiments.....	10
Figure 3. Photos of the Al sample holder used in D ₂ O-vapor-conditioning experiment.	10
Figure 4. Experimental setup of in-situ study of the growth of vanadate inhibitor film under epoxy.....	11
Figure 5. (a) NR data from e-beam deposited AA2024. (b) Best-fit SLD profile corresponding to the solid line through the data points in (a).....	15
Figure 6. (a) XR data from as-prepared bare AA2024. (b) Best-fit SLD profile corresponding to the solid line through the data points in (a).....	16
Figure 7. (a) XR data from as-prepared bare AA2024. (b) Best-fit SLD profile corresponding to the solid line through the data points in (a).....	16
Figure 8. (a) XR data from a layered Al-Cu sample before (red dots) and after (blue triangles) annealing. (b) Best-fit SLD profile of annealed sample corresponding to the solid blue line through the data points in (a).	17
Figure 9. (a) XR data from as-prepared thick AA2024 (around 2 μm). No fringes were observed indicating a rough surface. (b) XR data from as-prepared vanadate inhibitor film grown on thick AA2024. The absence of fringes limits the amount of information that can be extracted from the XR profiles.....	18
Figure 10. (a) XR data from V films after 30-s (red circles) and 60-s (blue triangles) precursor solution treatment in the as-prepared dry state. (b) Best-fit SLD profile of inhibitor film after 30-s precursor solution treatment corresponding to the solid red line through the data points in (a).19	
Figure 11. (a) NR data from V films made from H ₂ O precursor solution. (b) Best-fit assuming a one-layer, uniform-SLD profile corresponding to the solid line through the data points in (a). The films were exposed to the inhibitor solution for 30 s. A two-layer model (Figure 13) fits considerably better.	19
Figure 12. (a) NR data from V films made from D ₂ O precursor solution. (b) Best-fit to a one-layer, uniform-SLD profile corresponding to the solid line through the data points in (a). The films were exposed to the inhibitor solution for 30 s.....	20
Figure 13. (a) NR data from V films made from H ₂ O precursor solution. (b) Best-fit two-layer, uniform-SLD profile corresponding to the solid line through the data points in (a). The low-SLD interface layer is required to fit the data adequately.	20

Figure 14. (a) NR data from V films made from D ₂ O precursor solution. (b) Best-fit two-layer, uniform SLD profile corresponding to the solid line through the data points in (a).	21
Figure 15. (a) NR data from V film when in as-prepared dry state (red circles) and at equilibrium with D ₂ O vapor (blue triangles). The solid lines through the data points are the best fits corresponding to the SLD profile in (b). (b) Best-fit SLD profiles.	21
Figure 16. (a) XR data from V film in as-prepared dry state. The solid lines through the data points are the best fits corresponding to the SLD profile in (b). (b) Best-fit SLD profile.....	22
Figure 17. (a) NR data from V film made from formulation without K ₃ Fe[CN] ₆ in as-prepared dry state. The solid lines through the data points are the best fits corresponding to the SLD profile in (b). (b) Best-fit SLD profile.	23
Figure 18. NR data from V film before (red dots) and after 200-°C conditioning in vacuum for 24 hours (blue triangles).	24
Figure 19. NR data from V film before (red dots) and after immersion in H ₂ O at room temperature for 24 hours (blue triangles).....	24
Figure 20. (a) NR data from epoxy coated V film in as-prepared dry state. The solid line through the data points is the best fit corresponding to the SLD profile in (b). (b) Best-fit SLD profile. .	24
Figure 21. NR data from epoxy coated AA2024 substrate.	25
Figure 22. Photo of pure copper substrate after exposure to V precursor solution.	25
Figure 23. (a) XR data from epoxy coated AA2024 substrate before (red dots) and after (blue triangles) V film growth experiment. (b) Photo of epoxy coated AA2024 substrate after exposed to V precursor solution.....	25
Figure 24. (a) SLD after 5 s immersion in H ₂ SO ₄ , (b) SLD after 15 s immersion in H ₂ SO ₄ , (c) SLD after 30 s immersion in H ₂ SO ₄ , (d) SLD after 1 min immersion in H ₂ SO ₄	27
Figure 25. (a) XR data for TCP film prepared by immersion. The line is the best fit to a 3-layer model. (b) SLD profile based on data in (a). Two TCP layers are observed on top a thinned Al-alloy layer.....	27
Figure 26. (a) The Al-alloy-coated wafer was anodically activated. The cathodic reaction is hydrogen evolution. (b) The wafer was then cathodically polarized to form a coating layer. The anodic reaction is presumably dissolution of the Zn electrode.	29
Figure 27. Pourbaix diagram of Cr. Cr(III) in solution becomes unstable when pH is above 3 if [Cr(III)] = 1 molar, (line 0)	30

Figure 28. (a) NR data of TCP film prepared by 1 min EA-deposition. (b) SLD profile based on data in (a). A dense interface and a porous top layer ($570 \pm 10 \text{ \AA}$) on Al-alloy are required to fit the data.	30
Figure 29. (a) NR data for TCP film prepared by 2 min EA-deposition. (b) SLD profile based on data in (a). The coating thickness is $1010 \pm 10 \text{ \AA}$	31
Figure 30. (a) NR data for TCP film prepared by 4 min EA-deposition. (b) SLD profile based on data in (a) with the thickest coating layer $1770 \pm 10 \text{ \AA}$	31
Figure 31. (a) NR data for TCP film prepared by 4-min EA-deposition after 30-min baking in 150 C° , (b) SLD profile after baking based on data in (a). The coating layer shrinks and condenses, (c) SLD of the sample before baking.	32

List of Acronyms

AA2024 aluminum alloy 2024

AA2024-T3 Heat-treated aluminum alloy 2024

CCC: Chromium conversion coating

CeCC: Cerium conversion coating

DI: Deionized (water)

EA-deposition: Electro-assisted deposition

LANL: Los Alamos National Laboratory

NR: Neutron reflectivity

PVD: Physical vapor deposition

SLD: Scattering length density

SPEAR: The Surface Profile Analysis Reflectometer at LANL

TCP: Trivalent chromium process

V film: Vanadate inhibitor film

XR: X-ray reflectivity

ZP: Zinc phosphate

Acknowledgement

This research is funded by a contract from the Strategic Environmental Research and Development Program.

Neutron reflectivity measurements were carried out at the Lujan Neutron Scattering Center (LANSCE) at Los Alamos National Laboratory (LANL), and the Spallation Neutron Source (SNS) at Oak Ridge National Laboratory (ORNL). X-ray reflectivity work was done at the Advanced Materials Characterization Center (AMCC) at the University of Cincinnati.

Work performed at Surface Profile Analysis Reflectometer (SPEAR) at Lujan Neutron Scattering Center was supported by LANL under DOE contract W7405-ENG-36, and by the DOE Office of Basic Energy Sciences. The Spallation Neutron Source at Oak Ridge National Laboratory is sponsored by the Scientific User Facilities Division, Office of Basic Energy Sciences, U.S. Department of Energy. Oak Ridge National Laboratory is managed by UT-Battelle, LLC, for the U.S. Department of Energy under contract DEAC05-00OR22725.

We thank Hillary Smith, Jaroslaw Majewski, Michael Jablin, Jim Browning, John Ackner, and Candice Halbert for their assistance in collecting the reflectivity data.

Section 1. Executive Summary

The nature of protective films formed by corrosion inhibitors has been controversial since such films were first postulated by Faraday in the 1840's. The problem is that conventional techniques are not able to resolve profiles of the chemical and physical properties normal to the substrate surface. Current understanding of protection and degradation, therefore, is largely based on electrochemical methods, which are not specific enough to discriminate between proposed mechanisms.

This limited-scope project demonstrates that neutron reflectivity (NR) and x-ray reflectivity (XR) can resolve the composition and structure of passive films formed by non-chromate inhibitors. Because this work represents the first application of reflectivity to corrosion science, a number of issues had to be addressed. Can sufficiently smooth metals substrates be fabricated? Can alloy substrates be fabricated? What is the impact of activation and cleaning on thin metal films? Is the thickness of inhibitor films matched to the resolution of reflectivity instruments? Are the films sufficiently smooth to measure composition profiles? What conditions are required to deposit optimum inhibitor films? Can film growth be measured under a topcoat? How do the films evolve in response to water and thermal conditioning? We carried out a series of experiments to address each of these questions.

Metal substrates: After considerable experimentation with Al-Cu deposition methods we found that AA2024 films could be deposited by e-beam evaporation of an AA2024-T3 ingot. We also created Al-Cu films by annealing of an Al-Cu layered structures, but did not further explore inhibition on these substrates. The optimum thickness of the metal substrate was found to be about 400 Å. Thicker films were too rough and compromised downstream data analysis.

Activation: We found that thin metal films are easily stripped during cleaning and surface activation. To find the optimum activation conditions, we observed the stripping of the oxide and underlying metal films as a function of acid exposure. Thirty-second exposure turned out to be the optimum treatment that stripped the oxide, but not the underlying metal.

Vanadium films: Thirty-second exposure to vanadate inhibitor solution produced a complex inhibitor film structure. A minimum of two inhibitor layers was required to fit the data. During deposition, the native alumina layer is stripped from the metal and the metal itself thins slightly.

Vanadate film growth from a formulation without $K_3Fe(CN)_6$ was characterized by NR to verify its accelerating effect. Although the fitting is not perfect, the analysis is sufficient to verify that $K_3Fe(CN)_6$ plays an important role to achieve thick, smooth, dense films.

If the dried films are exposed to water vapor, the water penetrates both layers. The equilibrium water volume fraction is 5% in the top layer and 18% in the interfacial layer. The hydrophilic interfacial layer is a potential vulnerability of the film. A 400-Å thick wetting layer was also observed on the air-side surface.

Based on the ratio of neutron to x-ray reflectivity, no composition of the type $V_2O_5 \cdot (H_2O)_x$ is consistent with the data. Assuming the inhibitor film only contains vanadium and oxygen, the atomic formulas for bottom and bulk top layers are VO and VO_7 respectively, neither of which is stoichiometric. The corresponding densities of bottom and bulk top layers are (3.00 ± 0.02) g/cm³ and (1.75 ± 0.02) g/cm³ respectively. If aluminum is also present in the V film as $V_xAl_2O_3$,

the calculated formula of bottom and top layers are $V_{3.5}Al_2O_3$ and Al_2O_3 with densities of $(3.00 \pm 0.02) \text{ g/cm}^3$ and $(1.75 \pm 0.02) \text{ g/cm}^3$ respectively.

Upon exposure to 200 °C for 24 h, vanadate films thin and densify considerably. The films also thin on exposure to liquid water. Both of these aging scenarios are considered desirable from a corrosion-inhibition perspective.

We also attempted to observe inhibitor film growth under an epoxy film. When exposed to full-strength vanadate precursor, however, the epoxy was severely degraded. At lower concentration, no change was observed at the metal-epoxy interface for exposures up to 90 min.

Attempts to grow vanadate films on Cu substrates failed in that the acidic inhibitor solution stripped the Cu from the silicon substrate.

Trivalent Chromium Process (TCP) Films: Films deposited using a commercial TCP recipe (diluted METALAST[®] TCP-HF from Chemetall) were successfully characterized by NR and XR.

Films deposited by simple immersion show a two-layer structure, but the morphology differs from the vanadate films described above. For TCP films, the top layer is porous and thin compared to the denser, thicker layer at the metal interface. The observed structure is consistent with the film-formation mechanism postulated in the literature for Cr(III) coatings. The driving force for film deposition comes from the rise in pH near the substrate surface. The Al alloy partially dissolves, triggering the precipitation and deposition of Cr(III) hydroxide. Layer I forms during the initial fast precipitation of Cr(III) hydroxide. The high availability of Cr(III) and substantial increase in pH lead to a dense hydrous oxide. Layer I, however, retards the dissolution of Al alloy and slows the consumption of hydrogen ions, leading to a drop in pH. The limited pH increase in stage-2 growth is related to the competition between Al(III) diffusion and electron transfer through film layer, which increase the pH, and hydrogen-ion replenishment from the solution, which decreases pH. Reduced pH and lower availability of Cr(III) in stage-2 results in a more porous layer II.

TCP films were also deposited using an electro-coating method. The films were first polarized anodically to strip the oxide and then polarized cathodically to deposit the inhibitor film. In contrast to the immersion samples, these EA-deposited samples show only one uniform coating layer. To achieve decent fitting, however, a very thin, dense, interface layer between the alloy and the film is required. Once the dense interface forms, the resistivity rises and the current drops, limiting further growth of the dense layer. Subsequent deposition leads to a porous film similar to the immersion case. Continued growth leads to thickness increase, but little change in density because the current is limited by the dense interfacial layer, which is unchanged on further deposition. This situation leads to continuous deposition of a uniform top layer.

The composition profile of TCP films is considerably altered on exposure to 150 °C. The best explanation is that the film thermally dehydrates, leading to thinning and densification of the film. Based on the changes during dehydration, the composition of the as-prepared TCP e-coat film is $Cr_2O_3 \cdot 4H_2O$.

EA-deposition produces denser, thicker inhibitor films than immersion. In the case of EA-deposition the dense interfacial layer between the metal and the TCP film is extremely thin. Consumption of hydrogen ions is controlled by an external power supply leading to stable,

uniform growth once the interfacial layer forms. Film thickness then depends on the time under cathodic polarization. The resulting film is denser and thicker than the immersion films.

Other inhibitors: We were unable to produce measureable films based on cerium or zinc phosphate.

The above observations on vanadate and TCP films illustrate that inhibitor films are considerably more complex than expected on the basis of simplified single-layer models found in the literature. Since the reflectivity curve can be calculated for any proposed model, these models can be directly compared with observations in a quantitative way. Thus, reflectivity data bracket possible mechanisms for inhibitor action.

List of All Film Systems Analyzed

Metal Substrate Films:

Pure aluminum thin film

Pure copper thin film

AA2024 thin film

AA2024 thin film activated by 40% (v/v) H_2SO_4

Layered Al-Cu alloy films after annealing

Vanadate Inhibitor Films

V film from H_2O precursor solution

V film from D_2O precursor solution

V film from H_2O precursor, conditioned in D_2O vapor

V film without $\text{K}_3\text{Fe}[\text{CN}]_6$

V film after vacuum baking

V film after immersion in H_2O and re-dried

V film under an epoxy top coating

Trivalent Chromium Process Films

TCP film by immersion

TCP film by EA-deposition

TCP film by EA-deposition after vacuum baking

Section 2. Objective

The objective for this project was to apply neutron reflectivity in an effort to understand thoroughly the morphology and mechanisms of environmentally benign inhibitor systems.

Section 3. Background

Although non-chromate protective films of some type must exist on corrosion-inhibited metals, film morphology and speciation has eluded characterization except in a few cases. The problem is that conventional techniques are not able to resolve both the chemical and physical characteristics of submicron films. Current understanding of corrosion performance, therefore, is largely based on indirect electrochemical methods. Morphological studies based on electron imaging and electron spectroscopies do exist, but these methods do not yield quantitative data that can be compared to models. Also, because of the limited penetration depth of electrons, there is little information on chemical speciation normal to the surface, even though such speciation is central to models of passivation.

The method of specular reflection of x-rays/neutrons from surfaces has existed as an experimental technique for almost sixty years. These methods have been extensively used for solving soft-matter problems like polymer mixing, but have not been applied to elucidate inhibitor mechanisms. The most important advantage of neutron and x-ray reflectivity is the ability to characterize and track the chemical and/or physical changes of passive films non-destructively, including those under water and/or organic coatings.

In both x-ray and neutron reflectivity, a beam of photons is directed at a surface (Figure 1) at an incident angle of less than 1° . Reflectivity, $R(q)$, defined as the intensity ratio between reflected and incident beams, is measured as a function of the normal component of the scattering vector, $q = (4\pi/\lambda)\sin\theta$, where θ is the angle-of-incidence on the wafer and λ is the wavelength. All measurements were done in the specular mode, where the angle of incidence is equal to the angle of reflectance.

For a uniform film, the reflectivity curve, $R(q)$, oscillates as a function of q . The so-called Kiessig fringes are caused by the interference of waves reflected from both interfaces of the film. When q is significantly far from the critical edge (the q at which the beam first penetrates the film), the layer thickness, d , can be estimated from the Δq spacing between the minima of two neighboring fringes, by $d = 2\pi/\Delta q$.

By fitting the $R(q)$ curve it is possible to determine the chemical composition and density profile within the film. The inversion to obtain the real-space film composition profile is simple for a single layer of constant composition such as is often postulated for inhibitor films. As it turns out, however, few of the films we studied fall into this class. Nevertheless, we were able to work out the density and speciation profiles in several systems by a series of samples prepared

from H₂O and D₂O precursors that we studied by both x-ray and neutron reflectivity. The remainder of the report describes in detail how we accomplished this task.

When the raw reflectivity data are inverted, the result is not a composition profile directly, but a scattering-length-density (SLD) profile. In the case of x-rays, the SLD is just the electron density, which is determined by the chemical composition and mass density. In the case of neutrons, the neutron SLD is also directly determined composition and density, but the relationship cannot be described as the “neutron density.” Therefore we use the more generic designation SLD profile to describe both neutron and x-ray data.

As an example, Figure 5a shows measured neutron reflectivity data for a film of aluminum alloy on an oxide-covered silicon wafer. Figure 5b is the resulting SLD profile with the Si, SiO₂, Al and Al₂O₃ layers identified.

To harvest detailed information from reflectivity data, it is necessary to achieve smooth films less than 2000 Å. The key unknown at the beginning of the project was whether we could actually make such films. In addition, we had to achieve smooth alloy substrates. As will be shown, we achieved excellent vanadate and trivalent chromium films. We also tried Ce and Zinc phosphate, but so far have not achieved films of sufficient quality.

Detailed description of the materials and methods are given in Section 4. The information is sufficiently detailed that the experiments can be duplicated. Readers interested primarily in the results and conclusions should proceed to Section 5.

Section 4. Materials and Methods

Detailed information regarding materials used in the project is provided in this section. The experimental design and data analysis methods are also discussed in detail. Several non-chromate corrosion-inhibiting formulations were tested and studied in depth.

4.1 Metal substrates

4.1.1 Silicon wafer

The silicon wafers used to host the metal substrates were one-side-polished single crystal (111) wafers with a thickness of 1 or 5 mm obtained from Wafer World, Inc. (West Palm Beach, FL. USA).

4.1.2 Pure Aluminum substrate

Pure aluminum thin films were physically deposited on silicon wafers as metal substrate by e-beam evaporation. The pure aluminum ingot (99.99%) was purchased from McMaster-Carr Supply Company (Aurora, OH. USA).

4.1.3 Pure Copper substrate

Pure copper thin films were physically deposited on Titanium-coated silicon wafers by e-beam evaporation as metal substrate. The pure copper ingot (99.99%) was purchased from McMaster-Carr Supply Company (Aurora, OH. USA).

4.1.4 Aluminum alloy (AA2024) substrate

AA2024 thin films were physically deposited on silicon wafers as metal substrate by e-beam evaporation. The Al2024-T3 ingot was purchased from McMaster-Carr Supply Company (Aurora, OH. USA). The composition of AA2024 is 3.8 to 4.9 Cu, 1.2 to 1.8 Mg, 0.3 to 0.9 Mn, 0.5 Si and Fe, 0.15 Zn and Ti, and 0.1 Cr on a wt% basis.

4.1.5 Substrate preparation

4.1.5.1 Wafer cleaning

The silicon wafers were cleaned by immersion in a freshly prepared “Piranha” solution at room temperature for 30 minutes. Piranha solution is a mixture of H₂SO₄ and 30% H₂O₂ at a volume ratio of 7:3. After immersion, the wafers were rinsed repeatedly with de-ionized (DI) water. The silicon wafers were ready for e-beam deposition of metal film after desiccation.

4.1.5.2 e-beam evaporation

Electron-beam evaporation is a physical vapor deposition (PVD) method. In a typical e-beam system, the deposition chamber is evacuated to a pressure of 10⁻⁴ Torr. The material to be evaporated is in the form of an ingot. An electron beam generated by field emission is accelerated to a high kinetic energy and focused towards the ingot. The kinetic energy of the electrons is converted into thermal energy as the beam bombards the surface. The surface temperature of the ingot increases resulting in the formation of a liquid melt. Although some of incident electron energy is lost in the excitation of x-rays and secondary emission, the liquid ingot material evaporates under vacuum. The vapor of ingot material then deposits on the substrate and forms a smooth thin film. The thickness of film is controlled by deposition time. The e-beam depositions were carried out at Advanced Materials Characterization Center at the

University of Cincinnati. The e-beam instrument is Temescal FC1800 e-Beam Evaporator, from Airco Temescal, USA.

4.1.6 Structure of AA2024 substrate

To understand the morphology and underlying protection mechanisms, the AA2024 substrate was measured by NR at room temperature in the as-deposited state to determine the baseline film structure. The AA2024-coated wafer was measured by neutron reflectivity. The experimental setup is shown in Figure 1.

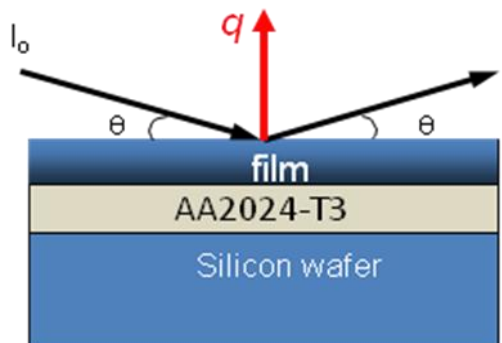


Figure 1. Experimental setup for specular NR/XR measurement in as-prepared dry state.

4.1.7 Optimization of the metal substrate

A series of experiments was carried out to find the optimum metal layer thickness. To achieve the high quality inhibitor films and to simplify the reflectivity data analysis, the thickness and smoothness of the metal substrate must be optimized. A thick metal film ($> 2000 \text{ \AA}$) simplifies the data analysis due to the elimination of interference signals from metal substrate. However, the roughness of metal layer also increases with thickness. A rough metal layer results in a rough inhibitor film, which complicates downstream data analysis. A thin metal film ($< 250 \text{ \AA}$) on the other hand can ensure smoothness but introduces the interference signals from metal layer itself and also complicates downstream data analysis. A long reaction time with the inhibitor solution leads to thick but rough films. A shorter reaction time results in a smoother film. A thin film, however, is possibly not representative of a functional inhibitor film.

Based on the above considerations, a series of samples were made by varying metal thickness and/or precursor treatment time. By measuring these samples by XR, optimized parameters were determined.

4.2 Characterization Methods

4.2.1 Neutron reflectivity (NR) and x-ray reflectivity (XR)

Neutron and x-ray reflectivity, the key technology used to reveal the film structure, are thoroughly discussed in the literature.[1-4] Therefore, only a brief description is given here.

The reflectivity, $R(q)$, defined as the intensity ratio between reflected and incident neutron/x-ray beam, is measured as a function of the scattering vector, $q = (4\pi/\lambda)\sin\theta$, where θ is the angle of incidence and λ is the neutron/x-ray wavelength. For the neutron measurements at SPEAR, Los Alamos National Laboratory, q was varied by collecting intensity for a range of wavelengths at a fixed angle of incidence. The incident wavelength distribution ranged from 1.4 to 16 \AA . The

reflectivity curves were obtained by merging data from two angles of incidence. Figure 5 (a) is an example of a measured R(q).

R(q) is determined by the scattering length density (SLD) profile normal to the surface of the sample. An example of an SLD profile is shown in Figure 5 (b). The SLD is a function of density and atomic composition. In case of neutrons:

$$SLD_{neutrons} = \rho \frac{N_A}{M} \sum_i b_i \quad (1)$$

Where b_i is the coherent scattering length of the i^{th} of atom, ρ is mass density, M is molecular weight, N_A is Avogadro's number. For x-rays, the SLD is proportional to average electron density and can be calculated by equation (2):

$$SLD_{x-ray} = \rho \frac{N_A}{M} \sum_{i=1}^{atoms} Z_i r_e \quad (2)$$

Where Z_i is the atomic number and r_e is the Thompson scattering length of an electron (classical radius). For a given material, the SLD is determined by chemical composition and mass density. The SLD of air is nearly zero due to the low density.

Although there is no simple relationship between R(q) and the SLD profile of the film, analysis code is available for a number of model film structures. We used “Parratt 32,” which is based on recursive Parratt formalism for multilayered structures.[1] To obtain agreement between the simulated and measured R(q), Parratt32 optimizes the parameters of a candidate real-space SLD profile by means of nonlinear regression. The simplest reasonable model is selected if more than one real-space model fits the data.

Neutron reflectivity experiments were carried out at using SPEAR at the Lujan Neutron Scattering Center, Los Alamos National laboratory and the BL-4B, Liquids Reflectometer at the Spallation Neutron Source at Oak Ridge National Laboratory. X-ray reflectivity measurements were carried out using a Phillips X'Pert PANalytical x-ray diffractometer at the Advanced Materials Characterization Center, University of Cincinnati.

4.2.2 X-ray diffraction

X-ray diffraction techniques are based on the elastic scattering of x-rays from structures that have long-range order. This technology was used to determine the composition and crystallinity of deposited inhibitor films. The measurements were carried out on Phillips X'Pert PANalytical x-ray diffractometer at Advanced Materials Characterization Center, University of Cincinnati.

4.3 Vanadate inhibition system

4.3.1 Formulation

The vanadate inhibitor coating formulation proposed by H. Guan and R.G. Buchheit was chosen as target formulation due to its simplicity and proven anticorrosion performance.[5] Analogous to the chromium inhibitor system, the precursor solution contains a mixture of NaVO₃ (10 mM), potassium ferricyanide (K₃Fe[CN]₆, 3 mM), and sodium fluoride (NaF, 2 mM) at room temperature. The bath pH was adjusted to 2.0 using concentrated HNO₃. In order to achieve a film suitable for neutron and x-ray reflectivity methods, a diluted (10 times) precursor solution was used.

4.3.2 Film growth procedure

Before application of the precursor solution, the metal-coated silicon wafers were rinsed repeatedly with acetone and de-ionized (DI) water to ensure a clean surface. After application of the inhibitor precursor solution on the metal surface for 30 seconds, the wafer is accelerated to 2000 rpm and held for 1 minute to spin off the excess solution. To get rid of the residual soluble components in the film, the samples were rinsed with DI water repeatedly and then dried in air at room temperature for 24 hours before further characterization. The coating procedure was carried out using a Laurell single-wafer spin processor (WS-400A-6NPP-Lite, North Wales, PA, USA).

4.3.3 Film study methods

4.3.3.1 Speciation of vanadate inhibitor film

According to Equation (1) and (2), the SLD of a material depends only on its atomic composition and mass density. Dividing Equation (2) by Equation (1), the ratio of x-ray and neutron SLD, Φ , is a function of atomic composition only:

$$\Phi = \frac{SLD_{x-ray}}{SLD_{neutron}} = \frac{\sum_{i=1}^{atoms} Z_i r_e}{\sum_{i=1}^{atoms} b_i} \quad (3)$$

Assuming that the base line formula of the vanadate inhibitor film is $V_2O_5 \cdot (H_2O)_x$ as proposed by Guan *et al.* [5], Equation (3) can be reduced to Equation (4).

$$\Phi = \frac{SLD_{x-ray}}{SLD_{neutron}} = \frac{2Z_V + 5Z_O + 2xZ_H + xZ_O}{2b_V + 5b_O + 2xb_H + xb_O} = \frac{2 \cdot 40.8 + 2 \cdot 8x}{2 \cdot 8.2 + 0.168x} \quad (4)$$

Equation (4) shows that Φ is an increasing function of x . The minimum value is 8.53, at $x = 0$, corresponding to no water in the film.

Once the speciation (x) is determined from the XR/NR SLD ratio, the density of the layer can also be calculated according to either Equation (1) or (2).

Samples were also made from a D_2O precursor solution to identify the baseline chemical composition. If the vanadate inhibitor film is not a hydrate, no neutron SLD difference should be observed in the SLD ratio for samples prepared from D_2O and H_2O .

4.3.3.2 Hydrophobicity of vanadate inhibitor films

The hydrophobicity is an important factor for anticorrosion performance. The hydrophobicity of vanadate inhibitor films was examined by NR on films exposed to saturated D_2O vapor. D_2O rather than H_2O is used to increase neutron contrast. The sample was sealed in an Al can with saturated D_2O atmosphere at room temperature for 12 hours to ensure the system reaches equilibrium. The thin wall of aluminum can is transparent to neutrons. By comparing the SLD profiles of the as-prepared dry state and water-vapor-conditioned state, the water response of vanadate inhibitor films can be determined.

Because the absorbed water usually resides in molecular-level free space inside the film,[6] the D₂O-equivalent volume fraction, ϕ_{D_2O} , can be calculated with Equation (5) assuming no swelling:

$$\phi_{D_2O} = \frac{SLD_{saturated} - SLD_{as-prepared}}{SLD_{D_2O}} \quad (5)$$

where the subscripts "saturated" and "as-prepared" mean the state of equilibrium with D₂O vapor and the virgin dry state.

In the presence of swelling or shrinking, Equation (5) is modified to Equation (6):

$$\phi_{D_2O} = \frac{SLD_{saturated} \times t_{saturated} - SLD_{as-prepared} \times t_{as-prepared}}{SLD_{D_2O} \times t_{saturated}} \quad (6)$$

where t is the thickness of the film.

The vapor conditioning experiment setup is shown in Figure 2. The open reservoir contains excess liquid D₂O to ensure a saturated D₂O vapor atmosphere. Photos of Al can are shown in Figure 3.

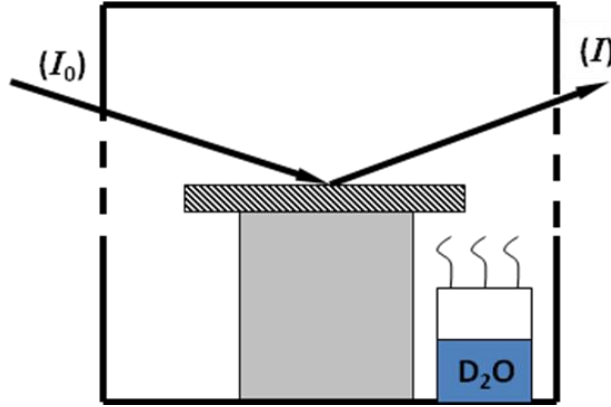


Figure 2. Experimental set up for “vapor conditioning” experiments



Figure 3. Photos of the Al sample holder used in D₂O-vapor-conditioning experiment.

4.3.3.3 Response to high temperature (200 °C)

In a practical service scenario, inhibitor films may see a high temperature environment. To understand the film response to elevated temperature, samples baked in an oven at 200 °C for 24 hours were measured by neutron and x-ray reflectivity. By following the strategies discussed in Section 4.3.3.1, the changes in the inhibitor film can be quantified.

4.3.3.4 Response to water immersion

The stability of inhibitor films under aqueous environment was determined by measuring the re-dried sample after immersion in liquid H₂O at room temperature for 24 hours.

4.3.3.5 Vanadate films under an epoxy top coating

Vanadate inhibitor films under an epoxy top coating were measured by NR in the as-prepared dry state. The film structure of vanadate inhibitor films was successfully determined without damaging the epoxy layer on top. This experiment demonstrated the capability of reflectivity technology as a non-destructive probe to determine the composition and structure of buried coating layers, which not possible by any other technique.

4.3.3.6 Growth of vanadate inhibitor film under epoxy on AA2024

To mimic the practical inhibitor scenario, an *in-situ* study of vanadate inhibitor film growth under epoxy on an Al alloy substrate was carried out by exposing the epoxy-coated substrate to a vanadate precursor solution. The experimental setup is shown in Figure 4. The sample was measured by NR every 15 min until no further change was observed. By tracking the SLD profile change, the growth of inhibitor film under epoxy can be observed.

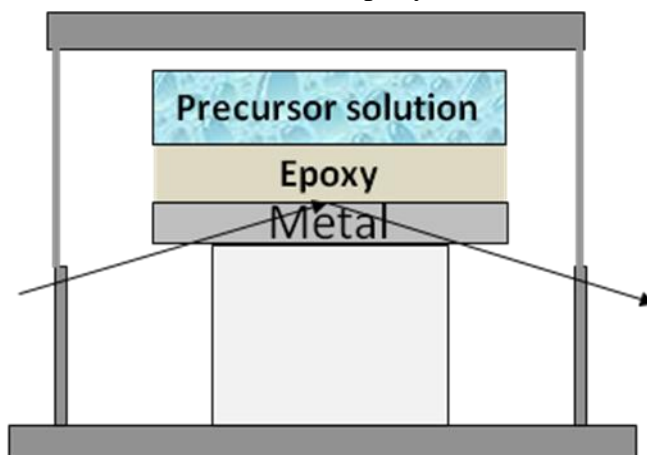


Figure 4. Experimental setup of in-situ study of the growth of vanadate inhibitor film under epoxy.

4.3.3.7 Vanadate inhibitor films on copper substrates

An attempt was made to grow a vanadate inhibitor film on a copper substrate following the same procedure as AA2024 (Section 4.1.3).

4.4 Trivalent chromium processing (TCP) system

4.4.1 Formulation

We used a commercial TCP product to make Cr(III) inhibitor film. The process includes a H_2SO_4 substrate pretreatment for activation. This pretreatment proved to be a critical step, so we studied the pretreatment process in detail. The TCP solution was METALAST® TCP-HF from Chemetall Oakite (2241 Park Place, Suite C Minden, NV)

H_2SO_4 was 95%-98% from Fisher Scientific. (Fair Lawn, New Jersey)

4.4.2 Film growth procedure

4.4.2.1 Electro-assisted (EA) deposition equipment

A DC power supply (CS11802X, 0-2 A, 0-18 V, adjustable DC regulated power supply, from Circuit Specialists Inc., 220 S Country Club Drive, #2 Mesa, AZ) was used to prepare EA-deposition samples.

4.4.2.2 Aluminum alloy (AA2024) substrate

Single crystal (111) wafers with a thickness of 1 mm and diameter of 5 in were used for AA2024 e-beam evaporation. The Al2024-T3 ingot was purchased from McMaster-Carr Supply Company. Deposited Al alloy film thickness is 400 Å. Alloy-coated wafers were cut in to small square pieces 1×1 inch for TCP coating and for Ce, ZP coating as well

4.4.2.3 Substrate activation

Al alloy-coated wafers were first activated in 40 % (v/v) H_2SO_4 at room temperature. XR analysis as a function of activation time revealed an optimum exposure time of 30 s.

4.4.2.4 TCP immersion

After 30-s activation in 40 % (v/v) H_2SO_4 , substrates were immediately rinsed but not dried and then immersed in 25% TCP film. This process did not exceed 5 s, in order to avoid reoxidation of fresh surface. The immersion time was 3 min. A TCP coating layer was noticeable after immersion. Samples were rinsed again and air-blown to dry.

4.4.2.5 TCP EA-deposition

For electro-assisted (EA) deposition experiment, a DC power supply was used. Acid activation was replaced by anodic polarization. Alloy-coated wafer was connected to the power supply as an anode, and immersed in 25% TCP solution. The cathode was placed in the solution also. Activation condition: 2V, 1 min (Figure 26a). After 1 min the voltage was switched from 2V to -3V; thus the wafer became a cathode. Three different coating times were chosen: 1 min, 2 min and 4 min. The coated samples were rinsed and air-blown to dry.

4.4.3 Response to high temperature (150 °C)

In a practical service scenario, TCP films may undergo a drying process for further condensation and dehydration. To understand the film response to elevated temperature, samples baked in an oven at 150 °C, 3×10^{-3} Torr, for 30 min. After baking, samples were measured by neutron reflectivity immediately.

Both TCP immersion samples and EA-deposition samples were chosen for this experiment.

4.4.4 Salt solution aging

Both TCP immersion sample and EA-deposited sample were studied as a function of aging. The aging conditions chosen were: 0.1 N NaCl solution for 6 h and 48 h. After aging immersion, samples were rinsed in DI water, blown to dry and further dried in room temperature for 1 h before neutron scattering.

4.5 Cerium inhibition system

4.5.1 Formulation

The cerium inhibitor system proposed by William G. Fahrenholtz from University of Missouri-Rolla was chosen.[7]

CeCl₃: Alfa Aesar, a Johnson Mathy Company (30 Bond street, Ward Hill, MA)

NaClO₄: from Alfa Aesar, a Johnson Mathy Company (26 Parkridge Road, Ward Hill, MA)

H₂O₂ (30%): from Fisher Scientific (2000 Park Lane Drive, Pittsburgh, PA)

DI Water: from Tedia Company Inc. (1000 Tedia Way, Fairfield, OH)

Formulation:	CeCl ₃	30 g
	NaClO ₄	120 g
	H ₂ O ₂ (30%)	2.2 g
	DI Water	600 ml

Substrate: 400 Å-thick Al 2024 coated Si wafer

Solution life: 1 h

Insoluble yellow substance gradually deposits after 1 hour. Once prepared, the solution should be used as soon as possible.

4.5.2 Film growth procedure

4.5.2.1 Aluminum alloy (AA2024) substrate

1 × 1 inch aluminum alloy-coated wafer pieces.

4.5.2.2 Substrate activation

30-s acid activation in 40 % (v/v) H₂SO₄ at room temperature.

4.5.2.3 Ce conversion coating

After 30-s activation substrates were immediately rinsed and immersed in Ce precursor solution. However a good conversion coating has not been achieved. No noticeable change was observed. Further immersion for longer time (6, 8, 10 min) was tried. After longer immersion, insoluble Ce sediments were observed instead of a Ce conversion coating. The sediments were easily washed off in the rinse process.

4.5.2.4 EA-deposition

EA-deposition experiment design was as similar as above for TCP EA-deposition. However anodic polarization produced pitting damage on the substrate. During the cathodic process Ce

species deposited only at the pitting area. Although different voltages (0.5V, 1V, 1.5V) and anodic polarization times (15 s, 30 s, 1 min) were tested, a uniform cerate film was not achieved.

Without anodic polarization, cathodic coating imparted no noticeable change of the substrate surface.

4.6 Zinc phosphate inhibition system (ZP system)

4.6.1 Formulation

One zinc phosphate (ZP) conversion coating formulation was tested, as it formed a very good ZP conversion coating layer on bulk Al (AA 2024) substrate in less than 1 min. The composition was:

H ₃ PO ₄ (85%)	16 ml (from Fisher Scientific, 2000 Park Lane Drive, Pittsburgh, PA)
ZnO	5.3 g (from Fisher Scientific, 2000 Park Lane Drive, Pittsburgh, PA)
NaF	0.5 g (from Fisher Scientific, 2000 Park Lane Drive, Pittsburgh, PA)
DI Water	600 ml

4.6.2 Film growth procedure

4.6.2.1 Aluminum alloy (AA2024) substrate

1 × 1 inch aluminum alloy-coated wafer pieces.

4.6.2.2 Substrate activation

30-s acid activation in 40 % (v/v) H₂SO₄ at room temperature.

4.6.2.3 ZP conversion coating

After 30 s-activation substrates were immediately rinsed and immersed in precursor solution. Coating behavior on alloy-coated wafer was quite different from bulk Al alloy. Only dissolution of Al alloy coating layer was observed. No conversion coating formed on wafer substrates.

Section 5. Results and Accomplishments

5.1 Substrate morphology

5.1.1 Objective and technical approach

Typical corrosion coupons are not suitable for reflectivity measurements. A key requirement to adapt reflectivity to corrosion science is to achieve metal substrates of sufficient smoothness to ensure high quality reflectivity data from inhibitor films deposited on the substrates. To this end a series of metal substrates were physically deposited on silicon wafers by e-beam evaporation as described in Section 4.1.5.2. The neutron and x-ray reflectivity characterizations were carried out following the strategies described in Section 4.2.1 and Section 4.2.2

As aerospace Al alloys are the primary substrates of concern, the morphology of aluminum alloy AA2024 film was studied in detail. In addition, annealing of layered Al-Cu was investigated as a possible route to Al-Cu alloys with tailored microstructure.

5.1.2 Project Accomplishments

5.1.2.1 Morphology of AA2024 substrate

After considerable experimentation with Al-Cu deposition methods we found that AA2024 films could be deposited by e-beam evaporation of an AAS2024-T3 ingot. Both the NR and XR results (below) show that the deposited film has the same composition and density as the alloy ingot used as the e-beam target.

The neutron reflectivity (NR) data on e-beam deposited AA2024 substrate are shown in Figure 5. The thickness of alloy is (400 ± 5) Å with a (30 ± 5) Å porous Al_2O_3 layer on top. The scattering length density (SLD) of bulk metal is $(2.13 \pm 0.05) \times 10^{-6} \text{ Å}^{-2}$, which is consistent with the calculated SLD based on the alloy's known density and atomic composition. The SLD of the porous oxide layer is $(3.8 \pm 0.3) \times 10^{-6} \text{ Å}^{-2}$, which is 66% as dense as solid Al_2O_3 .

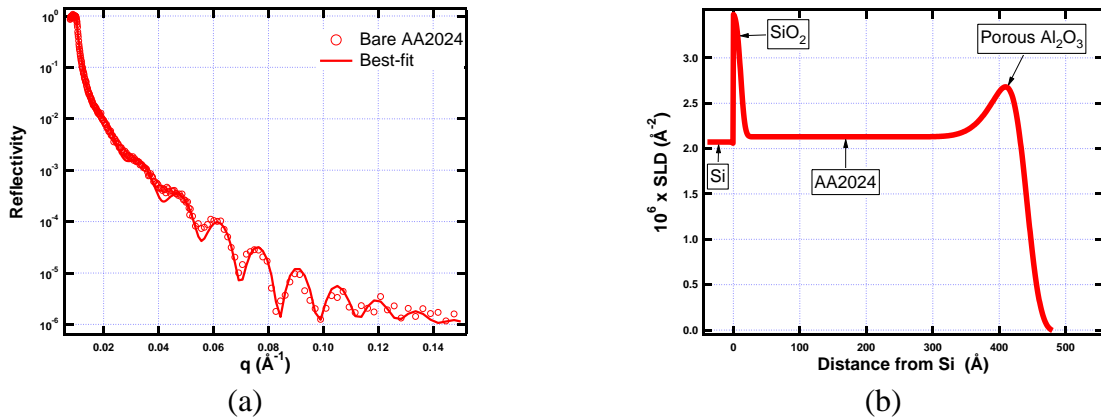


Figure 5. (a) NR data from e-beam deposited AA2024. (b) Best-fit SLD profile corresponding to the solid line through the data points in (a). Presumably the film is a laterally uniform solid solution.

The corresponding x-ray reflectivity (XR) data for AA2024 substrate are shown in Figure 6. The x-ray SLD profile indicates the same structure as found by NR (Figure 5). The x-ray SLDs

of bulk AA2024 layer and top oxide layer are $(23.5 \pm 0.5) \times 10^{-6} \text{ \AA}^{-2}$ and $(26.0 \pm 0.5) \times 10^{-6} \text{ \AA}^{-2}$ respectively.

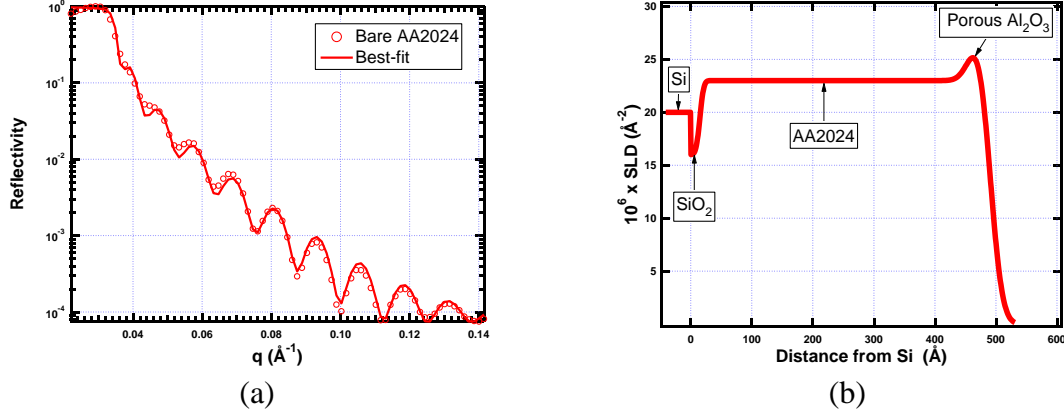


Figure 6. (a) XR data from as-prepared bare AA2024. (b) Best-fit SLD profile corresponding to the solid line through the data points in (a).

5.1.2.2 Morphology of pure copper substrate

We also investigated deposition and annealing of sequentially layered pure metals as a route to Al Alloys. Because of the success of the direct alloy deposition described in 5.1.2.1, however, we did not use these alloys for inhibitor studies. Nevertheless, the information gathered on the pure-metal method will be useful in future investigations of the impact of Cu content on the structure and mechanism of inhibitor films.

Deposition of pure Cu was proved to be more difficult than Al since Cu does not wet the Si wafer. To deposit Cu, a titanium buffer layer ($63 \pm 5 \text{ \AA}$) was first deposited on the wafer to aid adhesion of Cu.

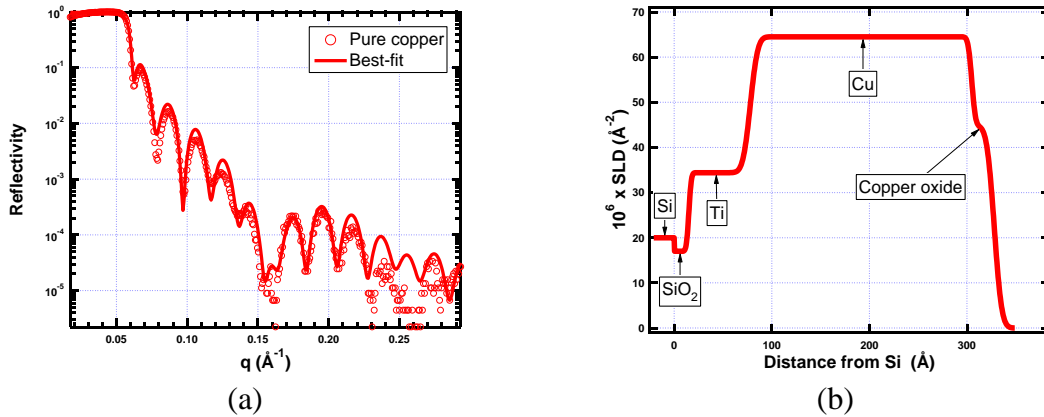


Figure 7. (a) XR data from as-prepared pure copper. (b) Best-fit SLD profile corresponding to the solid line through the data points in (a).

Cu deposits nicely on the Ti buffer layer. The XR of pure copper on Ti is shown in Figure 7. The thickness of copper is $(227 \pm 5) \text{ \AA}$ with a $(23 \pm 5) \text{ \AA}$ thick copper oxide layer on top. The x-ray SLDs of bulk copper layer and top oxide layer are $(64.5 \pm 0.5) \times 10^{-6} \text{ \AA}^{-2}$ and $(44.8 \pm 0.5) \times 10^{-6} \text{ \AA}^{-2}$ respectively. The SLDs of the two layers are consistent with the theoretical values.

5.1.2.3 Annealing of layered Al-Cu alloy films

In an attempt to create an e-beam deposited alloy film with tunable microstructure, the annealing of a layered Cu-Al system was observed by XR. A thin layer of Cu (100 Å) was deposited on top of 200-Å pure Al layer. The vacuum annealing protocol followed (300 °C for 15 hours followed by 450 °C for 5 min) was proposed by Nancy A. Missert (Sandia National Laboratories), a leading expert on the physics of metals.

The XR data before and after annealing are compared in Figure 8 (a). Figure 8 (b) gives the SLD profile of annealed sample. A SLD gradient normal to the surface was observed in the alloy film, which indicates the Cu and Al ingredients are not uniformly distributed. Nevertheless, Cu penetrates the entire Al layer. The SLD of Al-enriched region just above silicon wafer is $(33.0 \pm 0.5) \times 10^{-6} \text{ Å}^{-2}$, which indicates the volume ratio of Al/Cu is 75/25. On the top surface, the SLD is $(40.0 \pm 0.5) \times 10^{-6} \text{ Å}^{-2}$, which indicates the volume ratio of Al/Cu is 58/42.

Considering the Cu content in AA2024 is 3.8-4.9 wt%, the above annealing procedure is adequate to transfer the layered pure Al and pure Cu in proper thickness ratio into uniform Al-Cu alloy. This experiment shows that it will be possible to investigate the impact of Cu content on inhibitor film structure, although such experiments have yet to be attempted.

Interestingly, a simple two-layer model cannot fit the un-annealed film. We have yet to find a structure that can reproduce the measured XR data.

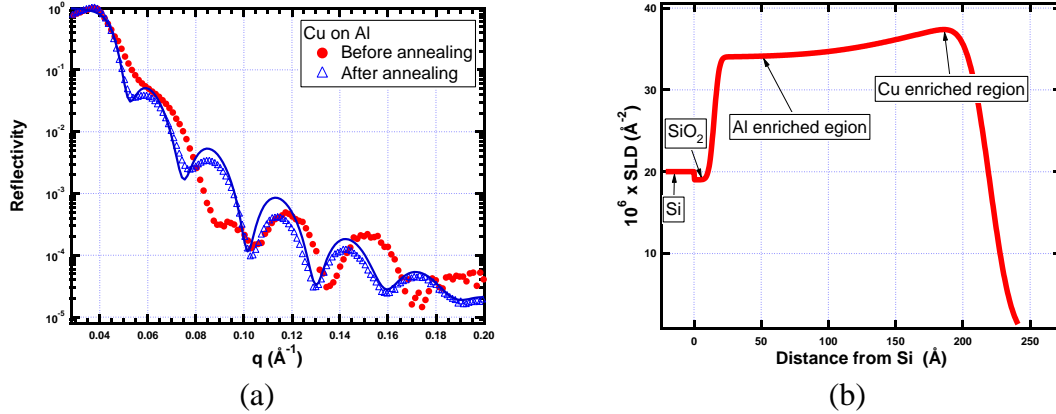


Figure 8. (a) XR data from a layered Al-Cu sample before (red dots) and after (blue triangles) annealing. (b) Best-fit SLD profile of annealed sample corresponding to the solid blue line through the data points in (a).

5.1.2.4 Metal substrate thickness optimization

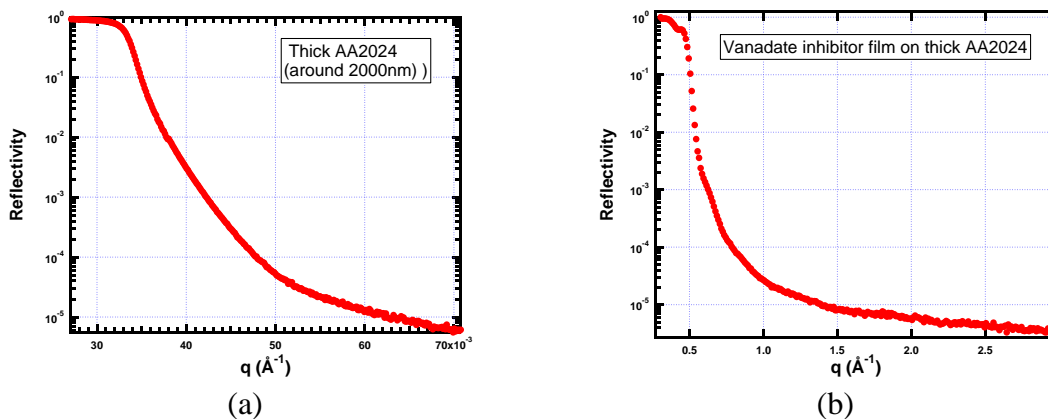


Figure 9. (a) XR data from as-prepared thick AA2024 (around 2 μm). No fringes were observed indicating a rough surface. (b) XR data from as-prepared vanadate inhibitor film grown on thick AA2024. The absence of fringes limits the amount of information that can be extracted from the XR profiles.

Following the procedure in Section 4.1.5.2, a thick AA2024 (around 2 μm) substrate was also prepared and characterized by XR. As shown in Figure 9 (a), the featureless curve without fringes indicates the film is too rough to be characterized by reflectivity. Data in Figure 9 (b) demonstrate that the rough surface of thick metal substrates results in a rough vanadate inhibitor film. The roughness is sufficient to wash out the fringes of the reflectivity curves. Therefore, a thick metal substrate does not provide the advantage hoped for in the downstream data analysis. We therefore used thin alloy films for subsequent inhibitor studies.

5.2 Inhibitor film structure

Inhibitor films were made from vanadate and chromium (III) formulations. The film structure and speciation were measured as well as the response of the films to water, high temperature and salt solution. Attempts to grow inhibitor films from cerium and zinc phosphate formulations were made, although no films suitable for reflectivity were achieved.

5.2.1 Vanadate inhibitor films (V films)

5.2.1.1 Precursor exposure optimization

V films prepared by 30-s and 60-s exposure to the vanadate precursor were measured by XR in the as-prepared dry state. As shown in Figure 10 (a), the XR data from the 30-s film has clear fringes (red circles), which indicates a smooth film. According to the SLD profile shown in Figure 10 (b), the total thickness of the inhibitor film is $(960 \pm 1) \text{\AA}$, which is in the desirable range for NR and XR. After 60 s of growth, however, the inhibitor film becomes thick and rough. The resulting reflectivity curve (blue triangles, Fig 10 (a)) primarily exhibits major fringes that arise from the alloy substrate. The signal from the inhibitor layer shows up as small fringes as marked in black circles on Figure 10 (a). The thickness estimated from the width of these fringes is $1890 \pm 10 \text{\AA}$, which is close to the upper limit detectable by NR. By comparing the two data sets, the 30-s exposure results in higher quality film than 60-s treatment, so 30-s exposure was used for subsequent experiments.

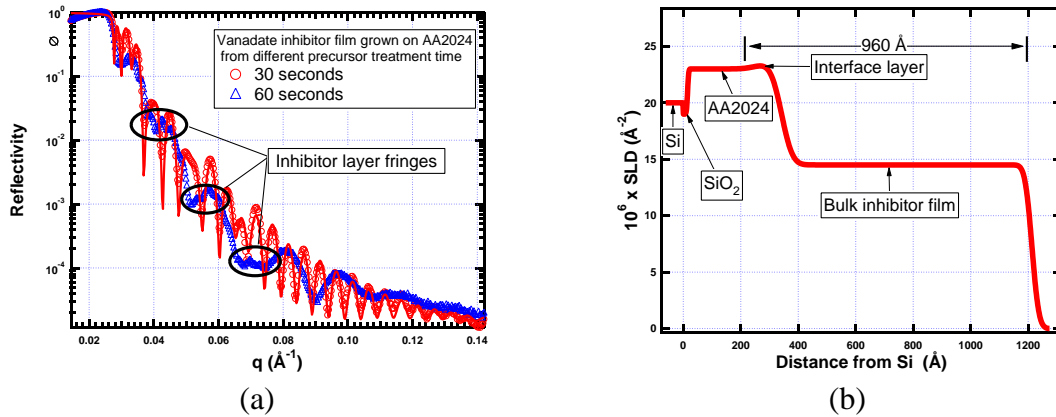


Figure 10. (a) XR data from V films after 30-s (red circles) and 60-s (blue triangles) precursor solution treatment in the as-prepared dry state. (b) Best-fit SLD profile of inhibitor film after 30-s precursor solution treatment corresponding to the solid red line through the data points in (a).

5.2.1.2 Film structure of V films

The virgin structures of V films made from H_2O and D_2O precursor solutions were examined by NR. The experimental setup is described in Section 4.2.

As shown in Figure 11 and Figure 12, a simple one-layer uniform inhibitor film model cannot fit the experimental data well. A layered model is required to get a credible fit to the reflectivity curves as shown in Figures. 13 and 14.

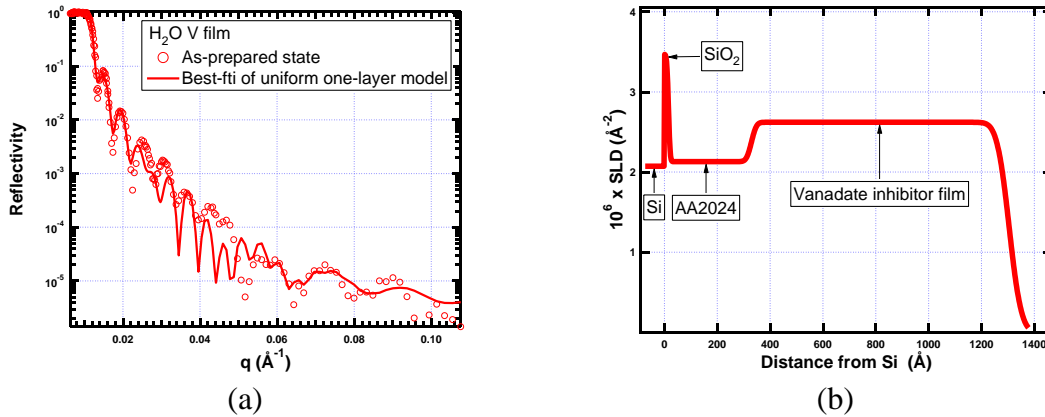


Figure 11. (a) NR data from V films made from H_2O precursor solution. (b) Best-fit assuming a one-layer, uniform-SLD profile corresponding to the solid line through the data points in (a). The films were exposed to the inhibitor solution for 30 s. A two-layer model (Figure 13) fits considerably better.

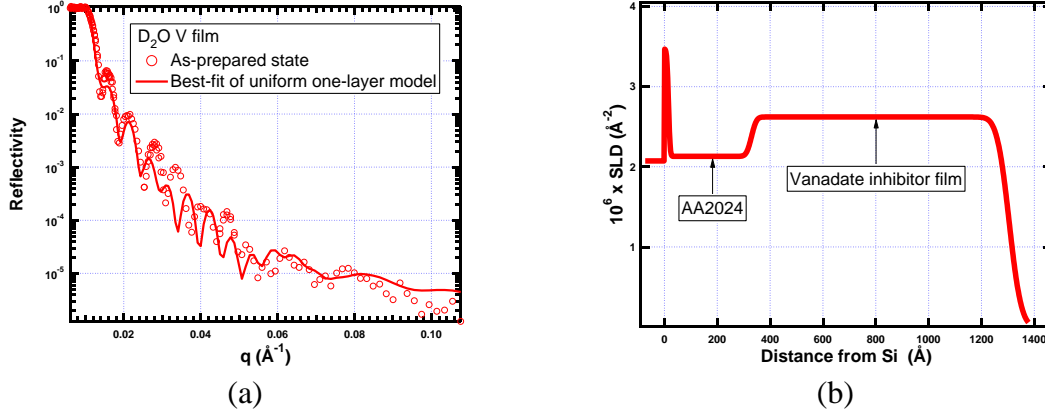


Figure 12. (a) NR data from V films made from D₂O precursor solution. (b) Best-fit to a one-layer, uniform-SLD profile corresponding to the solid line through the data points in (a). The films were exposed to the inhibitor solution for 30 s. Fitting with a two layer vanadate films is considerable better (Figure 13).

For H₂O-solution-prepared sample the bottom layer is $(95 \pm 5) \text{ \AA}$ with the top layer $(990 \pm 5) \text{ \AA}$ accounting for the rest of thickness. The neutron SLD of bottom layer is $(1.45 \pm 0.05) \times 10^{-6} \text{ \AA}^{-2}$, while the top layer is $(2.60 \pm 0.05) \times 10^{-6} \text{ \AA}^{-2}$. The roughness of top surface is around 40 Å.

As shown in Figure 14 (b), the D₂O-solution-prepared sample has a similar structure to the H₂O-solution-prepared case. The thickness of bottom and top layers are $(95 \pm 5) \text{ \AA}$ and $(880 \pm 5) \text{ \AA}$ respectively. The SLDs of the layers are the same as H₂O-solution-prepared sample. The roughness of top surface is also around 40 Å. As discussed below, the thin low-SLD bottom layer is more hydrophilic than the top layer.

For both samples, the thickness of AA2024 substrate is less than the virgin metal film and no aluminum oxide layer is observed, which indicates the top part of AA2024 layer is stripped by the precursor solution.

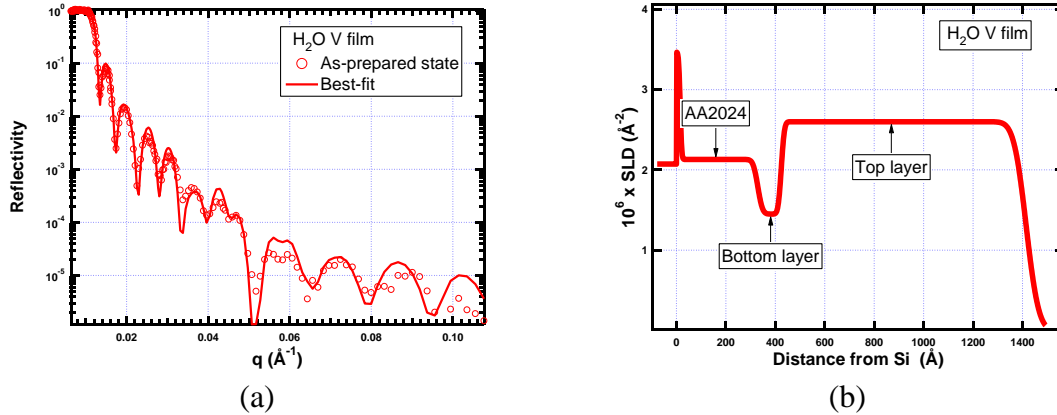


Figure 13. (a) NR data from V films made from H₂O precursor solution. (b) Best-fit two-layer, uniform-SLD profile corresponding to the solid line through the data points in (a). The low-SLD interface layer is required to fit the data adequately.

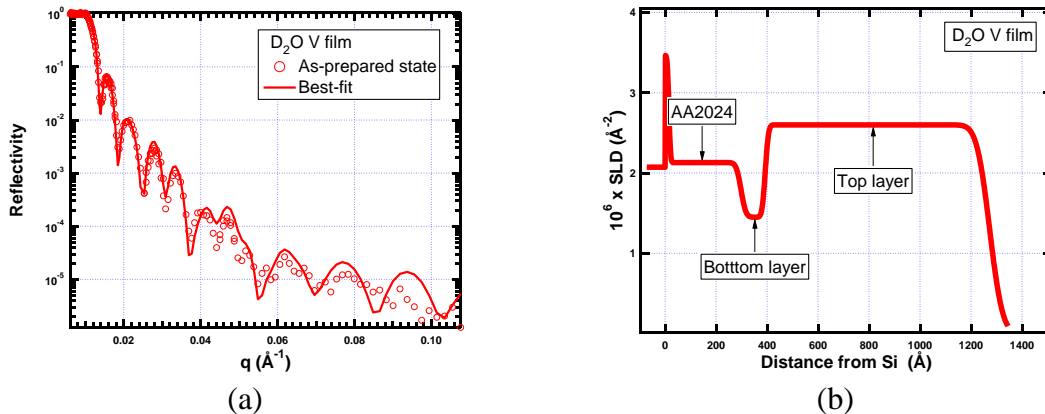


Figure 14. (a) NR data from V films made from D₂O precursor solution. (b) Best-fit two-layer, uniform SLD profile corresponding to the solid line through the data points in (a).

5.2.1.3 Porosity and hydrophobicity of V film

D₂O vapor conditioning experiments were carried out for V films. The reflectivity curves from the as-prepared film and the same film exposed to saturated D₂O vapor at room temperature for 12 hours are shown in Figure 15(a). D₂O rather than H₂O is used for these experiments since it has better contrast than H₂O and much less incoherent scattering. Because the vanadate film is too thin for optimum data analysis, experiments are planned to repeat these experiments on thicker films.

On water exposure the reflectivity increases relative to the as-prepared film due to the absorption of D₂O. At equilibrium, water penetrates the entire film. The SLD of the saturated bulk film increases from $(2.60 \pm 0.05) \times 10^{-6} \text{ Å}^{-2}$ to $(2.90 \pm 0.05) \times 10^{-6} \text{ Å}^{-2}$, implying the D₂O volume fraction is 5.0%. For the bottom layer, the SLD increases from $(1.45 \pm 0.05) \times 10^{-6} \text{ Å}^{-2}$ to $(2.60 \pm 0.05) \times 10^{-6} \text{ Å}^{-2}$, implying the D₂O volume fraction is 18%. A D₂O wetting layer is also observed at the air-side surface with a thickness of $(410 \pm 10) \text{ Å}$. There is no significant film swelling so water is absorbed in existing porosity. These results indicate the V film is not a water barrier.

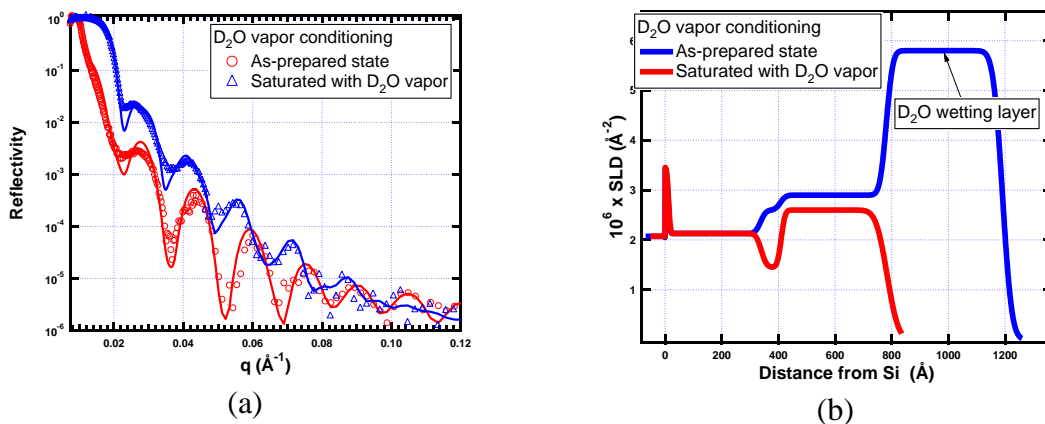


Figure 15. (a) NR data from V film when in as-prepared dry state (red circles) and at

equilibrium with D₂O vapor (blue triangles). The solid lines through the data points are the best fits corresponding to the SLD profile in (b). (b) Best-fit SLD profiles.

Because the water is mainly harbored in the molecular-level free space within the film,[6, 8] it is reasonable to assume that the porosity of the film equals to the water volume fraction at equilibrium. Therefore, the V film is more porous at the metal-film interface, which introduces a potential vulnerability to the V inhibitor system.

5.2.1.4 Speciation of V film

Since the ratio of x-ray to neutron SLDs is determined only by the atomic composition, the film composition can be calculated by combining XR and NR results as discussed in Section 4.3.3.1. The XR curve and best fit of V film are shown in Figure 16. The SLDs of bulk film and interfacial layer are $(14.5 \pm 0.5) \times 10^{-6} \text{ \AA}^{-2}$ and $(24.5 \pm 0.5) \times 10^{-6} \text{ \AA}^{-2}$ respectively. Therefore, the SLD ratios of x-ray to neutron of bulk top layer and interfacial bottom layer are 5.6 ± 0.3 and 17 ± 1 respectively.

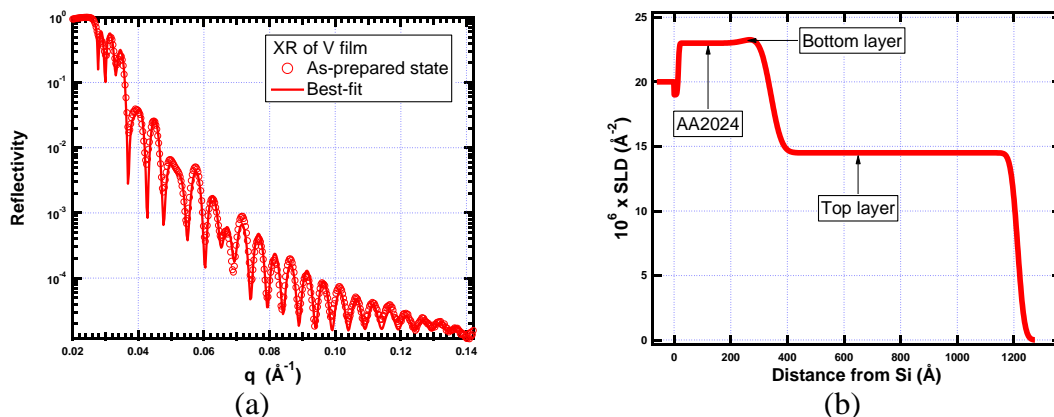


Figure 16. (a) XR data from V film in as-prepared dry state. The solid lines through the data points are the best fits corresponding to the SLD profile in (b). (b) Best-fit SLD profile.

Since the D₂O-solution-prepared and the H₂O-solution-prepared samples have the same neutron SLD for both bottom and top layers as discussed in Section 5.2.1.2, the speciation of V film cannot be a hydrate. That is the baseline formula of the V film must be different from the one Guan et al. proposed ($\text{V}_2\text{O}_5 \cdot (\text{H}_2\text{O})_x$). [5, 9]

The thin bottom layer, which is essential to fit the reflectivity data adequately, is not aluminum oxide, which has an SLD ratio of 5.85. The native oxide is stripped and the metal layer thins to 100 Å during deposition.

Assuming the inhibitor film only contains vanadium and oxygen, the atomic formulas for bottom and bulk top layers are VO and VO₇ respectively, neither of which is stoichiometric. The corresponding densities of bottom and bulk top layers are $(3.00 \pm 0.02) \text{ g/cm}^3$ and $(1.75 \pm 0.02) \text{ g/cm}^3$ respectively. If aluminum is also present in the V film as $\text{V}_x\text{Al}_2\text{O}_3$, the calculated formula of bottom and top layers are $\text{V}_{3.5}\text{Al}_2\text{O}_3$ and $\text{V}_0\text{Al}_2\text{O}_3$ with densities of $(3.00 \pm 0.02) \text{ g/cm}^3$ and $(1.75 \pm 0.02) \text{ g/cm}^3$ respectively. More work is required to rectify these issues.

5.2.1.5 Effect of $K_3Fe(CN)_6$

$K_3Fe(CN)_6$ is used as an accelerator for the Cr^{6+}/Cr^{3+} - Al^0/Al^{3+} redox couple in the chromate conversion coating system.[10] To determine the impact of $K_3Fe(CN)_6$ a formulation without $K_3Fe(CN)_6$ was characterized by NR. As shown in Figure 17 (b), only a (40 ± 10) Å V film formed on the AA2024 substrate. The average SLD of V film is $(1.0 \pm 0.4) \times 10^{-6} \text{ Å}^{-2}$, which is substantially lower than the film made from full recipe as described in Section 4.3.1. The roughness of the V film is comparable to its thickness. Although the fit in Figure 17 is not perfect, the analysis is sufficient to verify that $K_3Fe(CN)_6$ plays an important role to achieve thick, dense films.

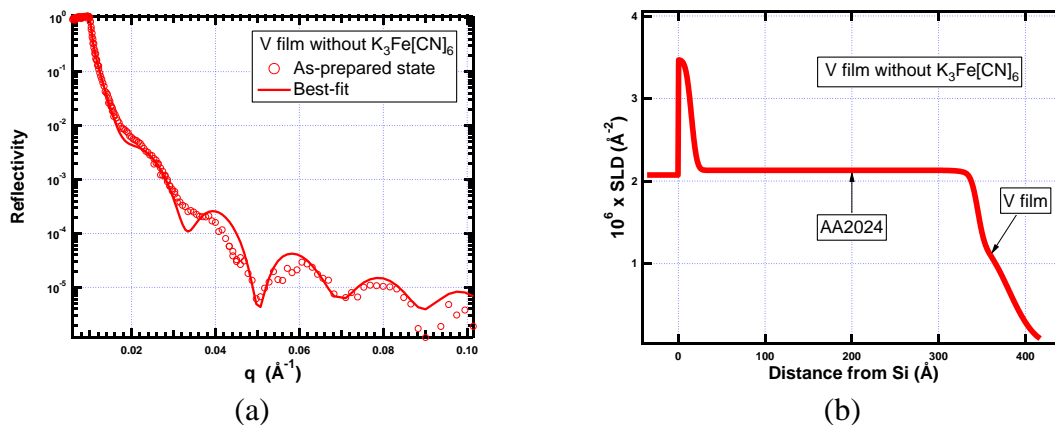


Figure 17. (a) NR data from V film made from formulation without $K_3Fe(CN)_6$ in as-prepared dry state. The solid lines through the data points are the best fits corresponding to the SLD profile in (b). (b) Best-fit SLD profile.

5.2.1.6 High temperature conditioning

Vanadate film before and after 200-°C conditioning in vacuum for 24 hours was characterized by NR to investigate its behavior at elevated temperature. As shown in Figure 18, the narrow fringes disappear after high temperature conditioning, which indicates the V film thins. As estimated from the fringe's width, the film thickness decreased from (730 ± 20) Å to (310 ± 20) Å. However, the reflectivity curve and the critical edge, $q_c = \sqrt{\pi \times SLD}$ (where neutron/x-ray beam begins to enter the film) shift to the right implying the SLD increases. Therefore, the V film after high temperature exposure is denser than the as-prepared film, which is preferred for metal protection.

5.2.1.7 Water immersion conditioning

After immersion in H_2O at room temperature for 24 hours, the V film was measured by NR in re-dried state. The changes in the V film are revealed by comparing the NR data before and after exposure as shown in Figure 19. As indicated by the arrow, the first dip shifts to the right implying the increased film SLD. According to the fringe-width increase, the film thickness decreased from (700 ± 20) Å to (630 ± 20) Å. The thinner-but-denser film after exposure to liquid water is preferred in terms of metal protection.

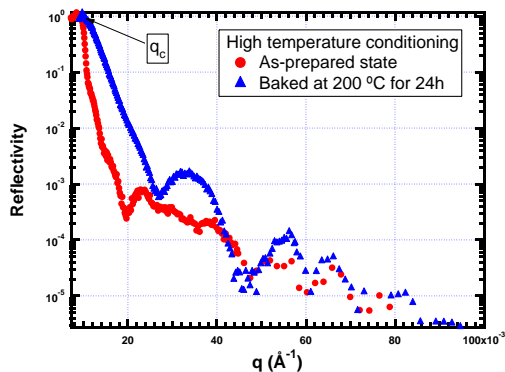


Figure 18. NR data from V film before (red dots) and after 200-°C conditioning in vacuum for 24 hours (blue triangles).

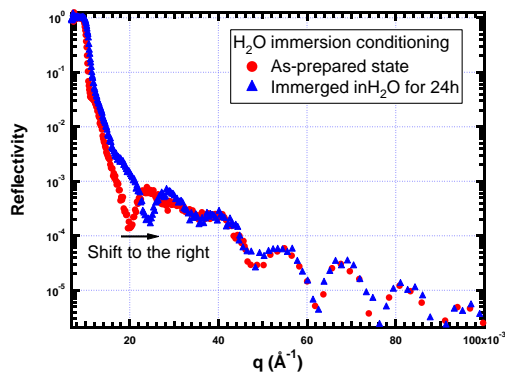


Figure 19. NR data from V film before (red dots) and after immersion in H₂O at room temperature for 24 hours (blue triangles).

5.2.1.8 V film under epoxy top-coating

The structure of buried V film was examined without damaging the epoxy top-coating by NR. Figure 20 gives the NR reflectivity curve and the corresponding SLD profile of V film under an epoxy top-coating. The layered V film structure as described in Section 5.2.1.2 is shown in Figure 20 (b). The epoxy layer is (680 ± 10) Å thick and has a SLD of $(1.4 \pm 0.05) \times 10^{-6}$ Å⁻². This experiment demonstrates the capability of NR to probe the buried coating layers non-destructively.

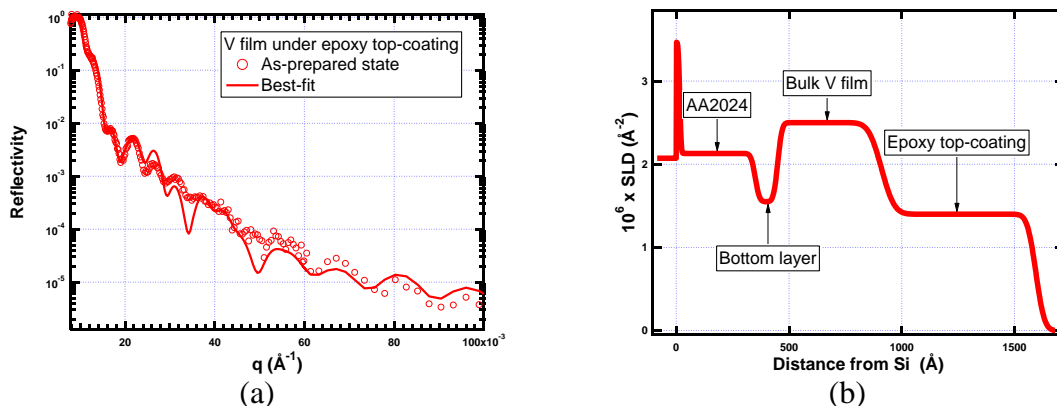


Figure 20. (a) NR data from epoxy coated V film in as-prepared dry state. The solid line through the data points is the best fit corresponding to the SLD profile in (b). (b) Best-fit SLD profile.

5.2.1.9 V film growth under epoxy on AA2024

An attempt to monitor film growth in-situ under epoxy on an AA2024 substrate was made according to Section 4.3.3.6. The epoxy coated AA2024 substrate was measured every 15 minutes while exposed to vanadate precursor solution. As shown in Figure 21, after 75 minutes exposure, no obvious changes were observed using a diluted precursor solution. An XR experiment with concentrated precursor (original concentration proposed by H. Guan and R.G.

Buchheit) was also carried out at University of Cincinnati by immersing the sample in the precursor bath instead of using NR liquid cell. The acidic precursor penetrates the edge of the wafer, resulting delamination of epoxy top-coating and consumption of the underlying AA2024 layer. Figure 23 (b) shows the photo of wafer after exposed to concentrated precursor solution for 30 minutes. The XR data after exposure (Figure 23 (a)) is featureless, implying rough silicon wafer surface.

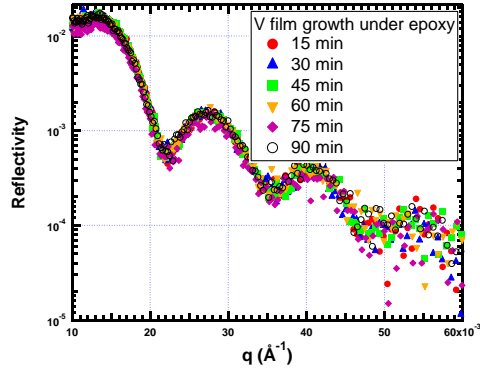


Figure 21. NR data from epoxy coated AA2024 substrate.



Figure 22. Photo of pure copper substrate after exposure to V precursor solution.

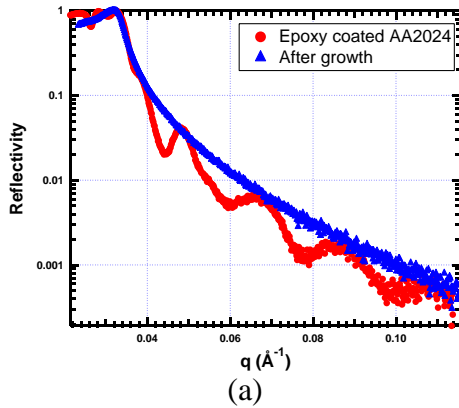


Figure 23. (a) XR data from epoxy coated AA2024 substrate before (red dots) and after (blue triangles) V film growth experiment. (b) Photo of epoxy coated AA2024 substrate after exposed to V precursor solution.

5.2.1.10 V film formation mechanism

Based on above results, we propose a highly simplified 4-stage process of the formation of V film on AA2024 as following.

First stage: Dissolution of metal surface. The acidic precursor dissolves the aluminum oxide and part of the aluminum, causing a slight increase of the pH near the metal surface.

Second stage: Fast precipitation. At elevated pH, vanadate precipitates from the solution and forms a thin hydrate layer and/or hydroxide gel. This layer forms in seconds and is relatively dense because of the high availability of vanadate ions and relatively high-pH environment compared with the next stage of film formation.

Third stage: Retarded growth. Because of the gel covering the metal surface dissolution of metal slows. The gel continues to polymerize leading to densification within the initial stage-2 gel layer, and further growth of a porous layer at the film-solution interface. The film growth ceases when densification halts the dissolution of metal. The layer formed at this stage is less dense and contains less vanadium than the bottom layer.

Fourth stage: Condensation. When the film dries the gel fully dehydrates, leading to an insoluble film containing complex compounds mainly of aluminum, vanadium and oxygen.

5.2.2 V film on Cu substrate

When vanadate precursor solution is applied on a Cu substrate, V film does not form as expected. The Cu substrate etched away and became rough. Figure 22 shows the photo of Cu substrate samples after exposed to vanadate precursor solution. For the thin (200 Å) copper substrate (Figure 23 a), the solution etched to the beneath Ti layer in seconds. For the thick (2000 Å) copper substrate (Figure 23 b), the solution stripped the copper layer and the surface became rough. No V film was observed.

5.2.3 Trivalent chromium process films (TCP films)

5.2.3.1 H₂SO₄ activation

H₂SO₄ activation of the metal surface is necessary before deposition of TCP films. Our Al alloy-coated wafers have only a 400 Å-thick Al coating, so the activation process has to be carefully controlled to avoid stripping the entire film. Therefore we measured the evolution of the metal substrate on exposure to 40 % (v/v) H₂SO₄. By comparing the XR data after immersion for 5 s, 15 s, 30 s, and 60 s, we observed the stripping of the native oxide followed by dissolution of the metal itself. Based on the XR SLD profile (Figure 24a), the oxide layer can still be identified after 5-s immersion. This alumina layer protects the underlying metal for about 30 s. The thickness of Al alloy layer changes little in this period (Figure 24 b), (c). Once alumina is completely consumed, the vulnerable Al alloy is exposed and dissolves quickly (Figure 24 d).

By comparing these four SLD profiles, passivation behavior of alumina layer is confirmed. In order to prepare a good conversion coating, this passivation layer must be removed before the subsequent immersion step. Due to the basic nature of the Al alloy, acid etching is so fast that its final thickness is hard to predict. Thus activation must cease before the alumina layer is completely removed. Thus 30 s was chosen as the optimized time for acid activation.

5.2.3.2 Film structure TCP immersion films

We have successfully prepared TCP films on Al-alloy-coated wafers by two methods, immersion and electroassisted (EA) deposition. In the immersion method, the alloy-coated Si wafers were first activated by immersion in 40 % (v/v) H₂SO₄ for 30 seconds. After activation, the rinsed wafer was immersed in 25 % (v/v) TCP solution (diluted METALAST[®] TCP-HF from Chemetall, 2241 Park Place, Suite C Minden, NV) for 3 minutes, rinsed and dried in air.

XR data for all samples prepared by immersion show a three-layer structure. The three layers are a) an Al-alloy layer, which is thinner than the native alloy layer, b) a middle film layer I, which is about 300-Å thick, and c) a top layer II, which has the lowest SLD, and is only 100-Å thick (Figure 25).

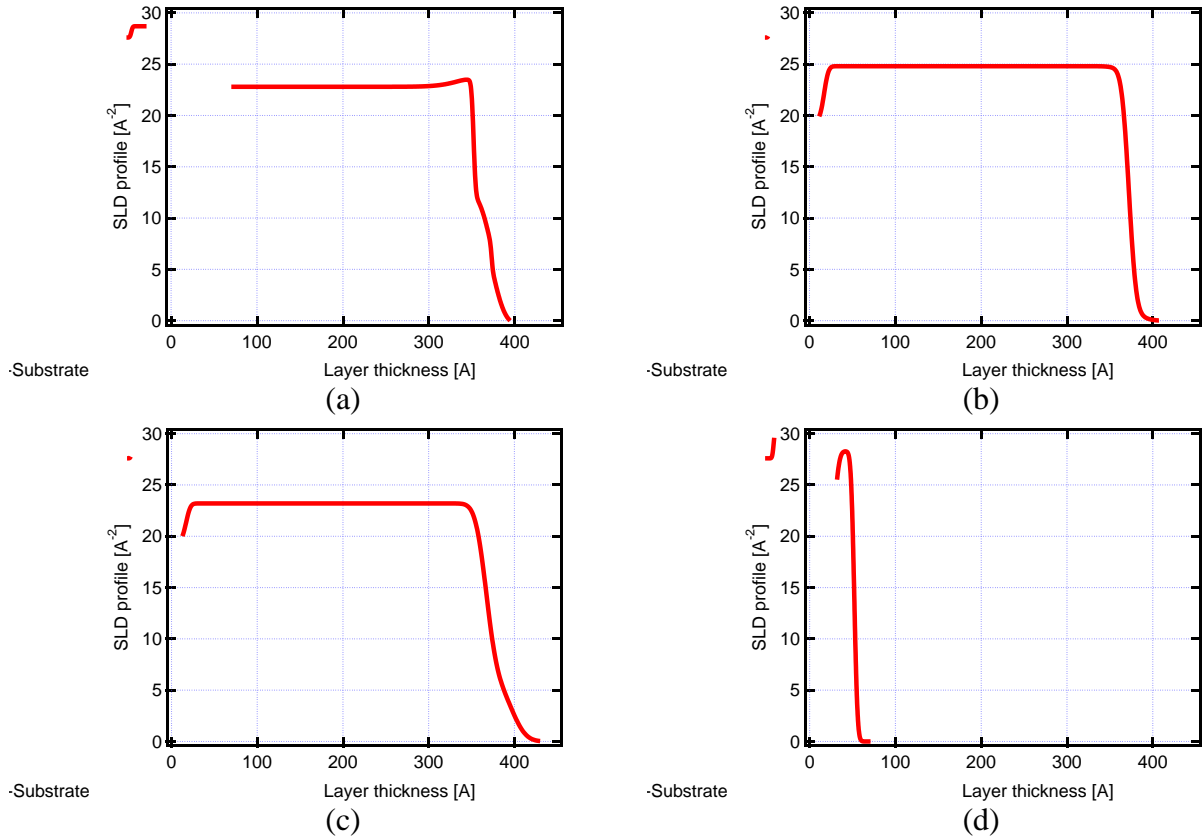


Figure 24. (a) SLD after 5 s immersion in H_2SO_4 , (b) SLD after 15 s immersion in H_2SO_4 , (c) SLD after 30 s immersion in H_2SO_4 , (d) SLD after 1 min immersion in H_2SO_4 .

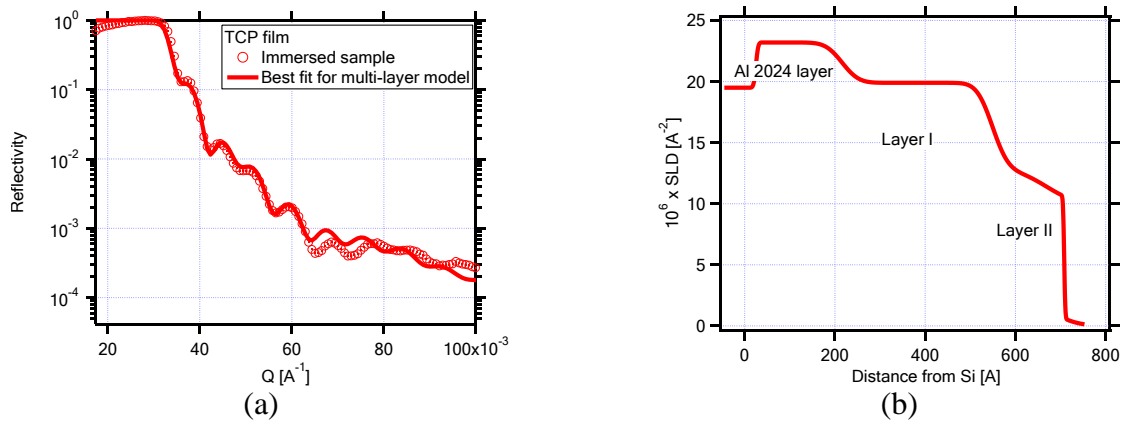


Figure 25. (a) XRD data for TCP film prepared by immersion. The line is the best fit to a 3-layer model. (b) SLD profile based on data in (a). Two TCP layers are observed on top a thinned Al-alloy layer.

The mass density, ρ , of the layers can be calculated from the SLD:

$$SLD_{x-ray} = \rho \frac{N_A}{M} \sum_{i=1}^{atoms} Z_i r_e \quad (2)$$

Where Z_i is the atomic number and r_e is the scattering length of an electron. For hydrated Cr(III) hydroxide, $Cr(OH)_3 \cdot nH_2O$:

$$\sum_{i=1}^{atoms} Z_i r_e = (103 + n \times 10) \times 0.28 \times 10^{-12} \text{ cm} \quad (7)$$

$$M = 103 + n \times 18 \text{ g/mol} \quad (8)$$

$$\rho = \frac{103 + n \times 18}{N_A \times (103 + n \times 10) \times 0.28 \times 10^{-12}} SLD_{x-ray} \text{ g/cm}^3 \quad (9)$$

Table I gives the density calculated from the measured SLD of layers I and II assuming $n = 0$ and 1. Note that the density is only weakly dependent on n . The density of fully condensed $Cr(OH)_3$ is 2.9 g/cm^3 .

Table 1. SLD and density of TCP film layer by immersion

	$10^6 \times SLD (\text{\AA}^{-2})$	Density (g/cm^3) ($n=0$)	Density (g/cm^3) ($n=1$)
Layer I	20.7 ± 0.2	2.48 ± 0.02	2.44 ± 0.02
Layer II	10.5 ± 0.2	1.26 ± 0.02	1.24 ± 0.02

The density of Layer II is only a half that of layer I, indicating the existence of pores or channels. The porous nature of layer II is less desirable from a corrosion-protection perspective. These results show that a uniform, thick film is difficult to obtain by immersion.

The observed structure is consistent with the film-formation mechanism postulated for Cr(III) conversion coating. [11] The driving force for film deposition comes from the rise in pH near the substrate surface. The Al alloy partially dissolves, triggering the precipitation and deposition of Cr(III) hydroxide. Layer I forms during the initial fast precipitation of Cr(III) hydroxide, stage-1. The high availability of Cr(III) and substantial increase in pH lead to a dense hydrous oxide. Layer I, however, retards the dissolution of Al alloy and slows the consumption of hydrogen ions, leading to a drop in pH. The limited pH increase in stage-2 is related to the competition between Al(III) diffusion and electron transfer through film layer, which increase the pH, and hydrogen-ion replenishment from the solution, which decreases pH. Reduced pH and lower availability of Cr(III) in stage-2 results in a more porous layer II. Multilayer TCP films have been reported on bulk Al alloy and Zn-coated steel. [11-13]

5.2.3.3 EA-deposition study of TCP films

In order to optimize TCP film for NR analysis, we developed a new EA-deposition method to control film growth. TCP involves two processes, which are separated in the e-coat method—a)

metal dissolution and pH increase and b) deposition of Cr(III) compounds. The advantage of EA-deposition is that deposition is controlled by voltage and/or current.

In the conventional immersion method, metal dissolution and Cr(III) deposition occur simultaneously, so Al(III) inevitably remains in the Cr(III) layer. Determination of the film composition from the SLD is compromised by the unknown amount of Al in the oxide layer. In the EA-deposition method, the two reaction stages are separated by polarizing the wafer anodically and then cathodically in TCP solution. Dissolution of Al layer does not take place in cathodic stage when the Cr(III) species deposits.

In order to dissolve the oxide layer, alloy-coated wafers are anodically polarized in the 25% TCP coating solution, at 2 V for 1 minute as illustrated in Figure 26. (a). The wafer is then cathodically polarized (Figure 26. (b)), at -3 V for 1, 2 or 4 minutes, so as to achieve different film thicknesses. After EA-deposition, the samples are rinsed and dried at room temperature.

When the wafers are anodically polarized, alumina and Al alloy dissolve at a controllable rate, which can be monitored by reading the current. Hydrogen bubbles are observed at the cathode. After 1-min polarization, the wafers are immediately switched to the cathode, so as to prevent oxidizing the fresh alloy surface. During the cathodic stage, excess electrons reach the wafer surface where they not only protect the Al alloy from oxidation but also react with hydrogen ions near the wafer surface leading local pH increase. So cathodic polarization triggers the precipitation and deposition of $\text{Cr(OH)}_3 \cdot n\text{H}_2\text{O}$ on the Al alloy surface (see Pourbaix diagram, Figure 27).

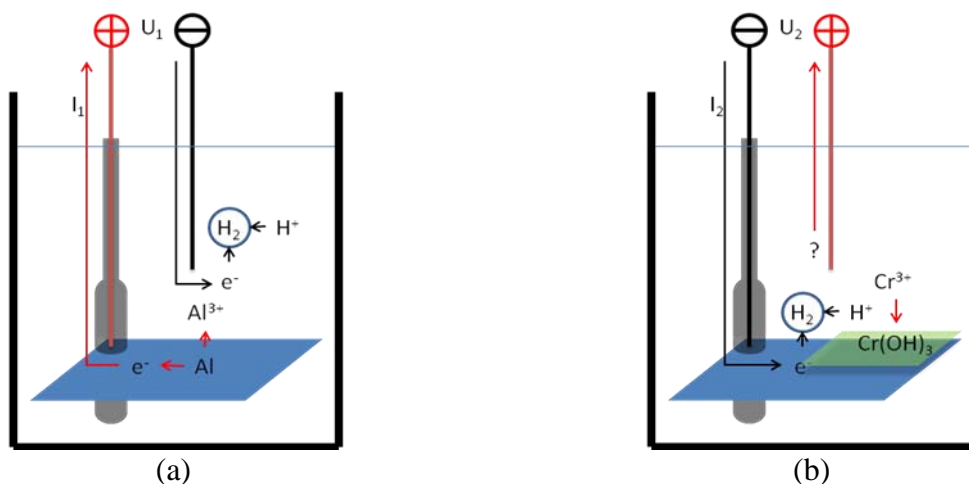


Figure 26. (a) The Al-alloy-coated wafer was anodically activated. The cathodic reaction is hydrogen evolution. (b) The wafer was then cathodically polarized to form a coating layer. The anodic reaction is presumably dissolution of the Zn electrode.

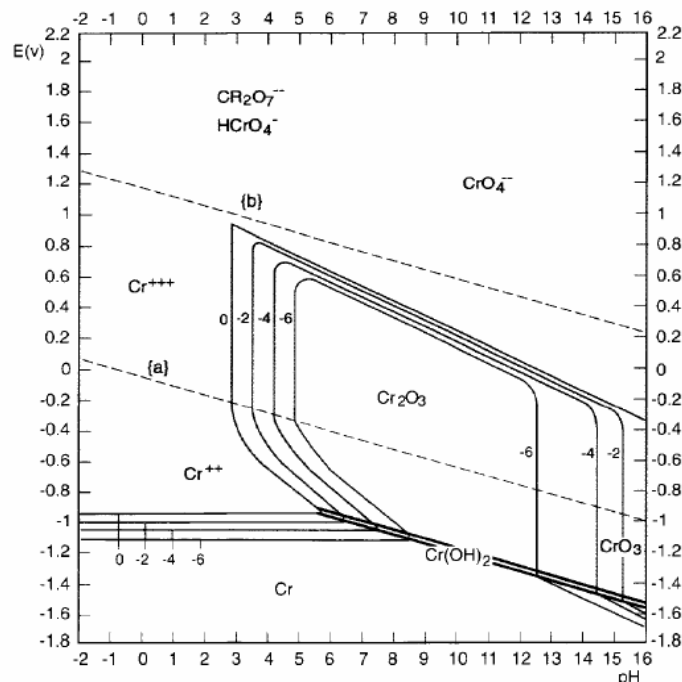


Figure 27. Pourbaix diagram of Cr. Cr(III) in solution becomes unstable when pH is above 3 if $[\text{Cr(III)}] = 1$ molar, (line 0) . (from Denny A. Jones, *Principles and Prevention of Corrosion*, 2nd edition, NY: Pearson-Prentice Hall)

Three EA-deposited samples were prepared with anodic polarization times of 1 min, 2 min and 4 min. Coating layers were smooth, gray and semi-transparent. Differences between the three samples were visually noticeable. Further NR analysis confirmed variation of coating thickness.

NR data of the three samples is shown in Figures. 28 - 30. By fitting the measured reflectivity curves a series of SLD profiles were obtained.

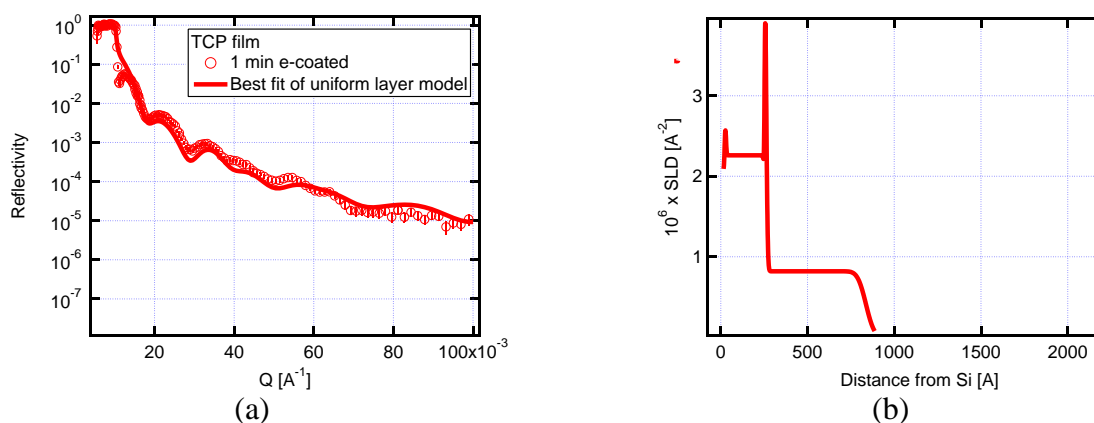


Figure 28. (a) NR data of TCP film prepared by 1 min EA-deposition. (b) SLD profile based on data in (a). A dense interface and a porous top layer (570 ± 10 Å) on Al-alloy are required to fit the data.

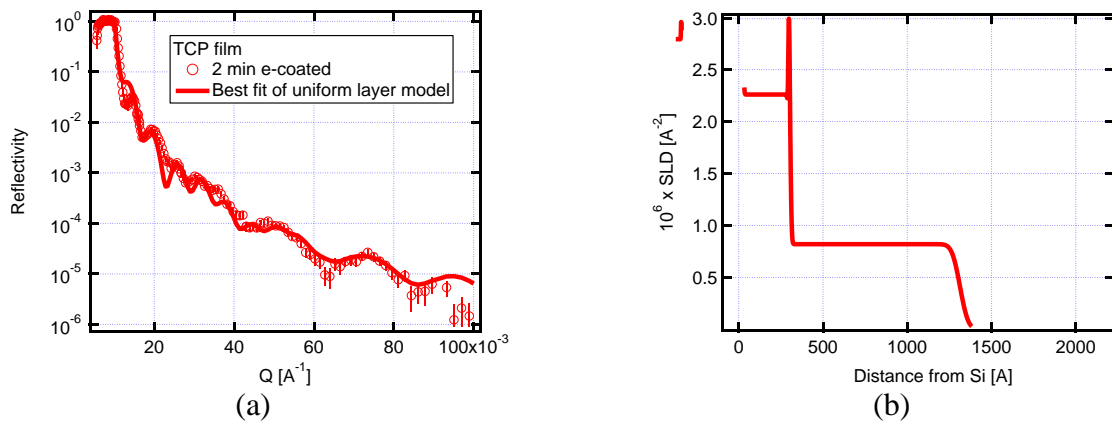


Figure 29. (a) NR data for TCP film prepared by 2 min EA-deposition. (b) SLD profile based on data in (a). The coating thickness is 1010 ± 10 Å

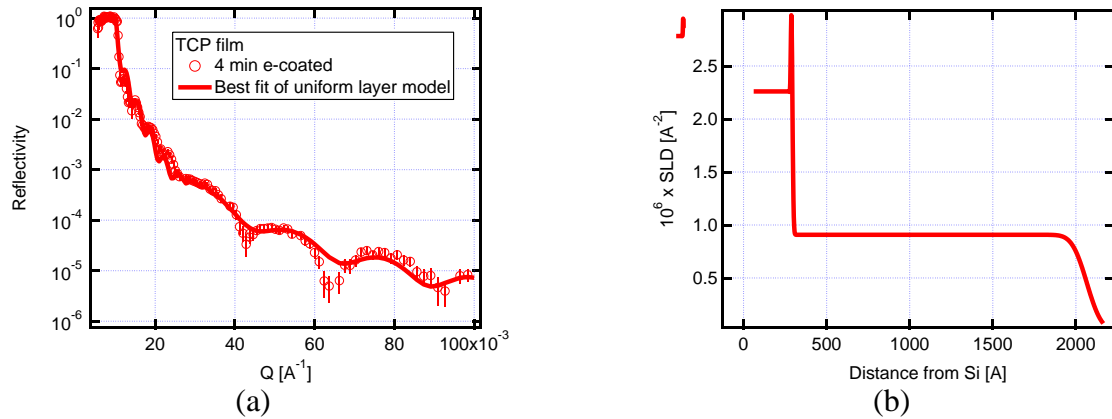


Figure 30. (a) NR data for TCP film prepared by 4 min EA-deposition. (b) SLD profile based on data in (a) with the thickest coating layer 1770 ± 10 Å.

Table 2. Thickness, neutron SLD and density of TCP ($\text{Cr}(\text{OH})_3 \cdot n\text{H}_2\text{O}$) by EA-deposition

EA-deposition time	thickness (Å)	$10^6 \times \text{SLD}$ (Å ⁻²)	Density (g/cm ³) (n=0)	Density (g/cm ³) (n=1)
1 min	570 ± 10	0.82 ± 0.02	1.40 ± 0.05	2.00 ± 0.05
2 min	1010 ± 10	0.82 ± 0.02	1.40 ± 0.05	2.00 ± 0.05
4 min	1770 ± 10	0.90 ± 0.02	1.55 ± 0.05	2.20 ± 0.05

These SLD profiles show different coating thicknesses, but all the coatings are much thicker than immersion-TCP films. Note that because these are neutron data, the density is a strong function of the assumed composition (Table 2).

In contrast to the immersion samples, these EA-deposited samples show only one uniform coating layer. To achieve decent fitting, however, a very thin, dense, interface layer between the

alloy and the film is required. The high- q data cannot be reasonably fit without this layer. Once deposition begins, however, the resistivity rises and the current drops, limiting further growth of the dense layer. Subsequent deposition leads to a porous film similar to the immersion case. Continued growth leads to thickness increase, but little change in density because the current is limited by the dense interfacial layer, which is unchanged on further deposition. This situation leads to continuous deposition of a uniform Cr(III) film.

5.2.3.4 High temperature conditioning

In order to study the dehydration of coating and calculate n in Table 2, baking experiments were completed. The 4-min sample was baked at 150 °C for 30 min and observed in NR. The SLD profile is substantially altered by the thermal exposure, Figure 31. (b), (c).

The increase of SLD can be explained by, a) film condensation, b) film dehydration. Film condensation is obvious, because thickness changes from 1770 Å to 980 Å. The coating became much thinner and SLD increased from $0.90 \times 10^{-6} \text{ Å}^{-2}$ to $2.27 \times 10^{-6} \text{ Å}^{-2}$. Thickness ratio between before baking and after baking is 1.8:1. However the SLD ratio after and before baking is 2.5:1, which is much higher than thickness ratio. As the SLD is proportional to film density, the simplest explanation is dehydration of the film.

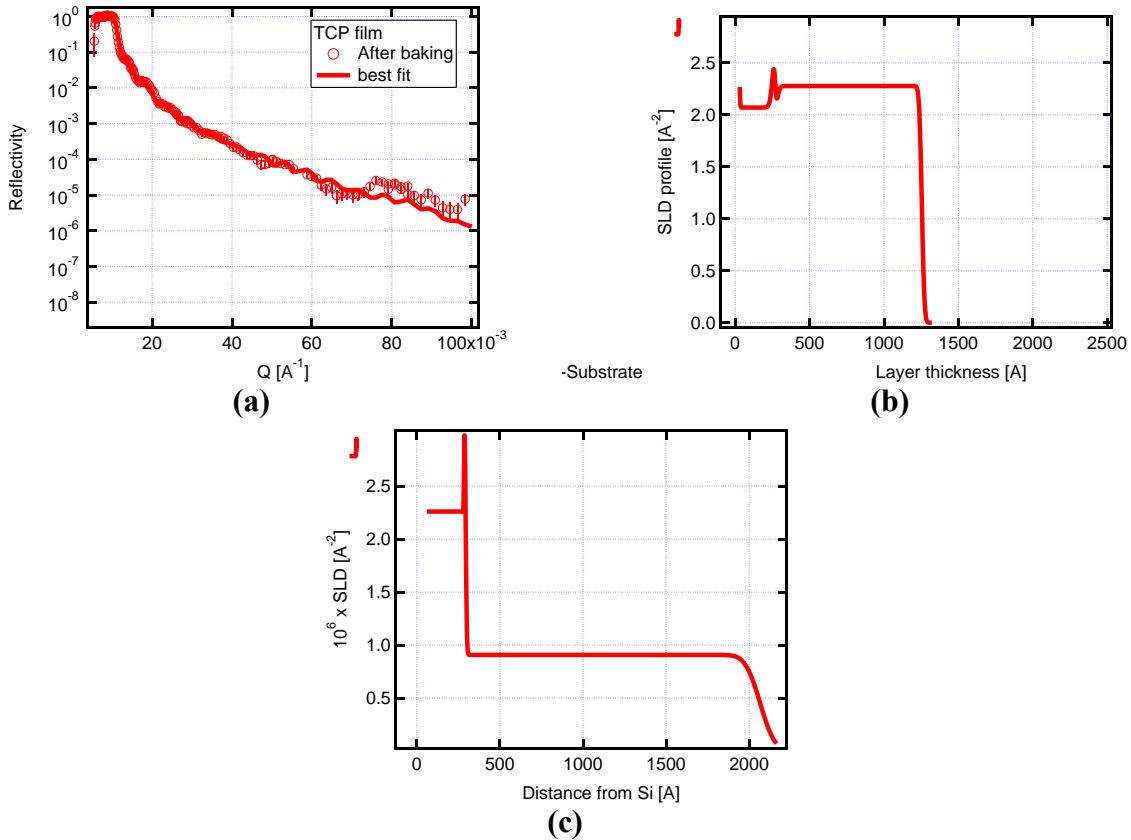


Figure 31. (a) NR data for TCP film prepared by 4-min EA-deposition after 30-min baking in 150 C°, (b) SLD profile after baking based on data in (a). The coating layer shrinks and condenses, (c) SLD of the sample before baking.

Table 3. Thickness, SLD of TCP EA-deposition film before and after baking

Coating thickness (Å)	$10^6 \times \text{SLD} (\text{\AA}^{-2})$	Assumed Cr(III) species	
$1770 \pm 10 \text{ \AA}$	0.90 ± 0.02	$\text{Cr}_2\text{O}_3 \cdot x\text{H}_2\text{O}$	before
$980 \pm 10 \text{ \AA}$	2.26 ± 0.02	Cr_2O_3	after

The level of hydration can be obtained from the SLD if we assume that $\text{Cr}(\text{OH})_3 \cdot n\text{H}_2\text{O}$ or $\text{Cr}_2\text{O}_3 \cdot x\text{H}_2\text{O}$ is the generic film composition in the TCP layer, and that, after baking, the film is Cr_2O_3 (Table 3).

Three equations (10, 11, 12) can be built in order to calculate n and x.

$$\text{SLD}_{\text{Cr}_2\text{O}_3 \cdot x\text{H}_2\text{O}} = \rho_1 \frac{N_A}{M_{\text{Cr}_2\text{O}_3 \cdot x\text{H}_2\text{O}}} \sum_{i=1}^{\text{atoms}} \text{Cr}_2\text{O}_3 \cdot x\text{H}_2\text{O} b_i \quad (10)$$

$$\text{SLD}_{\text{Cr}_2\text{O}_3} = \rho_2 \frac{N_A}{M_{\text{Cr}_2\text{O}_3}} \sum_{j=1}^{\text{atoms}} \text{Cr}_2\text{O}_3 b_j \quad (11)$$

$$\left[\rho_2 \frac{N_A}{M_{\text{Cr}_2\text{O}_3}} \sum_{j=1}^{\text{atoms}} \text{Cr}_2\text{O}_3 b_j \right] \times V_{\text{after}} = \left[\rho_1 \frac{N_A}{M_{\text{Cr}_2\text{O}_3 \cdot x\text{H}_2\text{O}}} \left(\sum_{i=1}^{\text{atoms}} \text{Cr}_2\text{O}_3 \cdot x\text{H}_2\text{O} b_i - x \times \sum_{k=1}^{\text{atoms}} \text{H}_2\text{O} b_k \right) \right] \times V_{\text{before}} \quad (12)$$

Equation (12) is conservation of total scattering length of Cr_2O_3 . V is the volume of uniform part of TCP film before and after baking, which is proportional to the layer thickness.

$$P_1 = \rho_1 \frac{N_A}{M_{\text{Cr}_2\text{O}_3 \cdot x\text{H}_2\text{O}}} \quad (13)$$

$$P_2 = \rho_2 \frac{N_A}{M_{\text{Cr}_2\text{O}_3}} \quad (14)$$

Where P_1 is molecule number density of TCP film species before baking and P_2 is the same after baking.

$$\sum_{i=1}^{\text{atoms}} \text{Cr}_2\text{O}_3 \cdot x\text{H}_2\text{O} b_i = 2.46 + x \times 0.167 \times 10^{-12} \text{ cm} \quad (15)$$

$$\sum_{j=1}^{\text{atoms}} \text{Cr}_2\text{O}_3 b_j = 2.46 \times 10^{-12} \text{ cm} \quad (16)$$

$$\sum_{k=1}^{\text{atoms}} \text{H}_2\text{O} b_k = 0.167 \times 10^{-12} \text{ cm} \quad (17)$$

$$0.90 \times 10^6 \text{ Å}^{-2} = P_1 \times (2.46 + x \times -0.167) \times 10^{-12} \text{ cm} \quad (18)$$

$$2.27 \times 10^6 \text{ Å}^{-2} = P_2 \times 2.46 \times 10^{-12} \text{ cm} \quad (19)$$

$$2.27 \times 10^6 \text{ Å}^{-2} \times 980 \text{ Å} = 2.46 \times 10^{-12} \text{ cm} \times P_1 \times 1770 \text{ Å} \quad (20)$$

$$2n+3=x \quad (21)$$

Eq. (18) ÷ Eq. (20) yields $x = 4$, $n=0.5$. The TCP layer after EA-deposition is mainly composed of $\text{Cr}(\text{OH})_3 \cdot 0.5\text{H}_2\text{O}$. Densities of the EA-deposited films are recalculated in Table 4.

Table 4. Thickness, SLD and density of TCP ($\text{Cr}(\text{OH})_3 \cdot 0.5\text{H}_2\text{O}$) by EA-deposition

EA-deposition samples	thickness (Å)	$10^6 \times \text{SLD}$ (Å ⁻²)	Density (g/cm ³)
1 min	570 ± 10	0.82 ± 0.02	1.65 ± 0.05
2 min	1010 ± 10	0.82 ± 0.02	1.65 ± 0.05
4 min	1770 ± 10	0.90 ± 0.02	1.85 ± 0.05
4 min baked	980 ± 10	2.26 ± 0.02	2.30 ± 0.05

Based on the above calculation, it can be reasonably assumed that the composition of the as-prepared TCP e-coat film is $\text{Cr}_2\text{O}_3 \cdot 4\text{H}_2\text{O}$ or $\text{Cr}(\text{OH})_3 \cdot 0.5\text{H}_2\text{O}$. Film density was adjusted (Table 4) according to the new value of $x = 4$.

5.2.4 Ce and ZP conversion coating films

We were unable to prepare Ce and ZP films of sufficient quality for XR and NR studies. The immersion method does not work for either Ce or ZP systems. Compared to reported film performance on bulk AA2024, there must be some unknown difference between AA2024-coated wafer and bulk AA2024. A possible explanation is that e-beam coating of AA2024 yields a uniform structure. However the bulk alloy has Cu-rich inclusions, which form cathodes and accelerate the coating process during immersion in the precursor solution.

EA-deposition method was also tried to deposit Ce and ZP films, but suitable coating conditions were not realized.

Section 6. Conclusions

6.1 Conclusions regarding substrate preparation

Metal substrates (Cu, Al and Al-Cu alloy) suitable for NR/XR technology can be made by e-beam evaporation. The optimum metal substrate thickness is around 400 Å. This thickness offers the best balance of the film quality and the ease of subsequent data analysis.

Substrates can also be prepared by annealing of layers Al-Cu films. The vacuum annealing protocol (300 °C for 15 hours followed by 450 °C for 5 min) is able to transform the layered pure Al and pure Cu in proper thickness ratio into uniform Al-Cu alloy with tunable microstructure.

6.2 Conclusions regarding Vanadate (V) films

Highest quality V film on AA2024 substrate was achieved with 30-s exposure to 1/10 diluted precursor solution. The top part of the AA2024 substrate anticipates the V film formation by dissolving into the precursor solution and locally raising up the pH above the metal substrate surface. $K_3Fe(CN)_6$ plays an important role in the formation of V film as an accelerator for the Al^0/Al^{3+} redox couple.

The typical thickness of V film formed on AA2024 under the experimental conditions is 800 - 1000 Å. A layered film structure is observed. The bottom thin (< 100 Å) layer at the metal-inhibitor film interface is more porous and hydrophobic than the bulk V film, which introduces potential vulnerability to the V inhibitor system.

The V film is not hydrated. That is the baseline formula of the V film is different from $V_2O_5 \cdot (H_2O)_x$. Vanadium is enriched at the metal-inhibitor film interface while the bulk layer is oxygen and Al enriched. If the V film contains only vanadium and oxygen, the calculated atomic formulas for bottom and bulk top layers are VO and VO_7 respectively. The corresponding densities are $(3.00 \pm 0.02) \text{ g/cm}^3$ and $(1.75 \pm 0.02) \text{ g/cm}^3$ respectively. If aluminum presents as $V_xAl_2O_3$, the calculated formula of bottom and top layers are $V_{3.5}Al_2O_3$ and Al_2O_3 .

The V film is not a water barrier. When treated with saturated water vapor, the water wets the air-side surface and penetrates the entire film. The absorbed water is harbored in the pre-existing molecular-level free space. However, when treated at elevated temperature or liquid water, the film becomes thinner but denser, which is preferred for inhibition applications.

The formation mechanism of V film is proposed as a four-stage process. The dissolution of metal increases the pH at the metal-precursor interface, which triggers the precipitation of vanadium species. The resulting gel retards subsequent deposition, resulting a layered structure. When the film dries the film fully dehydrates and forms an insoluble protective film.

The capability of probing buried inhibitor films was demonstrated by non-destructive determination of V film structure under epoxy top coating. No inhibitor layer grows under and uncompromised epoxy top coat even though the inhibitor solution is known to penetrate the epoxy layer.

6.3 Conclusions regarding TCP films

The structure of TCP films depends on how they are deposited. Immersion films are different from EA-deposited films in that the latter show a dense interface layer that retards subsequent film formation and limits film thickness. In both cases, the formation of TCP film is closely tied to rate of hydrogen consumption near the substrate surface. In the conventional immersion experiment, the hydrogen consumption is driven by the metal dissolution; however metal dissolution is inevitably restricted by the inhibitor film itself. Metal-ion diffusion through the film becomes increasingly difficult as the film grows. Thus dissolution is retarded and proton consumption is replenished by ions from the bulk solution. The pH drops leading to a thin, less-dense top layer.

EA-deposition produces denser, thicker inhibitor films than immersion. In the case of EA-deposition the dense interfacial layer between the metal and the TCP film is extremely thin. Consumption of hydrogen ions is controlled by an external power supply leading to stable, uniform growth once the interfacial layer forms. Film thickness then depends on the time under cathodic polarization. The resulting film is denser and thicker than the immersion films. The composition of the film is $\text{Cr}(\text{OH})_3 \cdot 0.5\text{H}_2\text{O}$ as determined by comparing the SLD before and after driving off the water of hydration.

These experiments represent the first measurements of the structure and composition of TCP films. The new data provides the first opportunity to learn exactly how films form and what the optimum structure is for corrosion protection. At this point it is not clear which film is most protective. The immersion film has a thicker dense layer, but is thinner and less dense overall. The EA-deposited films, on the other hand, have an extremely thin dense layer, but are overall thicker and denser. If SERDP decides to continue this project, we will complement the above structural measurements with corrosion and electrochemical data to solve this puzzle.

References

1. Parratt, L.G., Phys. Rev. Lett., 1954. **95**(2): p. 359-369.
2. Roe, R.-J., *Methods of X-ray and Neutron Scattering in Polymer Science*. 2000, New York: Oxford University Press.
3. Russell, T.P., *THE CHARACTERIZATION OF POLYMER INTERFACES*. Annu. Rev. mater. Sci., 1991. **21**: p. 249-268.
4. Russell, T.P., *On the reflectivity of Polymers: Neutrons and X-rays*. Physica B, 1996. **221**: p. 267-283.
5. Guan, H. and R.G. Buchheit, *Corrosion protection of aluminum alloy 2024-T3 by vanadate conversion coatings*. Corrosion, 2004. **60**(3): p. 284-296.
6. Wang, Y., et al., *Water absorption and transport in bis-amino silane films, in Silanes and Other Coupling Agents*, K.L. Mittal, Editor. 2008, VSP: Leiden, Netherlands.
7. Fahrenholtz, W.G., et al., *Characterization of cerium-based conversion coatings for corrosion protection of aluminum alloys*. Surface & Coatings Technology, 2002. **155**(2-3): p. 208-213.
8. Wang, Y., et al., *Water-Barrier Properties of Mixed Bis-[trimethoxysilylpropyl]amine and Vinyl Triacetoxysilane Films* Journal of Physical Chemistry, B, 2007. **111**: p. 7041-7051.
9. Livage, J., *Sol-gel chemistry and electrochemical properties of vanadium oxide gels*. Solid State Ionics, 1996. **86-8**: p. 935-942.

10. Zhang, W., *Formation and corrosion inhibition mechanisms of chromate conversion coatings on Al and AA2024-T3*, in *Materials Science and Engineering*. 2002, Ohio State University: Columbus, OH.
11. Wen, N.T., et al., *Microstructure of trivalent chromium conversion coating on electrogalvanized steel plate*. *Electrochemical and Solid State Letters*, 2008. **11**(8): p. C47-C50.
12. Cho, K.R., V. S.; Kwon, H., *Microstructure and electrochemical characterization of trivalent chromium based conversion coating on zinc*. *Electrochim Acta*, 2007. **52**(13): p. 4449-4456.
13. Yu, H.C., B.; Shi, X.; Sun, X.; Li, B., *Investigation of the trivalent-chrome coating on 6063 aluminum alloy*. *Materials letters*, 2008. **62**: p. 828-2831.